Protein kinase CK2α' as a dual modulator of immune signaling and synaptic dysfunction in Tauopathy

Angel White[1], Peter Gavrilyuk[1], Rafael Falcon Moya[1], Reid Thurston[1], Amal Fickak[1], Nicholas B Rozema[1], Prarthana Keshavaram[1], Scott Vermilyea[1], Riley Schlichte[1], Joyce Meints[1], Ying Zhang[2], Alfonso Araque[1], Michael Lee[1], Rocio Gomez-Pastor[1]

[1]University of Minnesota, School of Medicine, Department of Neuroscience.

[2]Minnesota Supercomputing Institute, University of Minnesota.

Abstract

Tauopathies are a group of neurodegenerative diseases characterized by tau accumulation, neuroinflammation, and synaptic dysfunction, yet effective treatments remain elusive. Protein Kinase CK2 has been previously associated with different aspects of tau pathology but genetic evidence for the contribution of CK2 to tauopathy remained lacking. Here, we show CK2α', one of the two catalytic subunits of CK2, as a novel regulator of tau-mediated neurodegeneration. We found that CK2α' expression is elevated in the hippocampus of PS19 tauopathy mice and in postmortem brains of dementia patients, particularly in neurons and microglia. Using genetic haploinsufficiency in PS19 mice, we demonstrated that reduced CK2α' levels significantly decrease phosphorylated tau and total tau burden in the hippocampus and cortex. CK2α' depletion also enhanced synaptic gene expression, synaptic density, and LTP, while attenuating microglial activation, synaptic engulfment, and pro-inflammatory cytokine levels. Importantly, CK2α' depletion rescued cognitive deficits assessed in the Barnes maze. These effects appear to be mediated through both neuronal and glial functions and may involve CK2α'-dependent modulation of tau-associated phosphorylation and neuroinflammatory and immune signaling pathways. Our findings highlight CK2α' as a key node at the intersection of tau pathology, synaptic dysfunction, and neuroimmune signaling. Targeting CK2α' may offer a novel and selective therapeutic strategy for modifying disease progression in tauopathies.

Introduction

Tauopathies encompass a broad range of neurodegenerative conditions, most notably Alzheimer's disease (AD) and related dementias (ADRD), for which no cure currently exists[1-3]. These disorders are generally categorized as either primary or secondary tauopathies. Primary tauopathies result from direct mutations in the microtubule-associated protein tau (MAPT), a protein critical for microtubule stabilization and intracellular transport[4,5]. In contrast, secondary tauopathies arise from pathological tau accumulation triggered by mutations in genes other than MAPT[6]. Regardless of the cause, tauopathies are typically marked by progressive neuronal loss, synaptic and cognitive dysfunction, and widespread inflammation in both the central nervous system and peripheral tissues[7-11]. A deeper understanding of the molecular mechanisms underlying tauopathies and their downstream consequences is essential for developing effective disease-modifying therapies. One key area of research is the role

neuroinflammation plays in the progression of tauopathies. These disorders are characterized by chronic, excessive inflammatory responses to abnormal tau proteins[8,9,12]. This persistent inflammation can exacerbate tau pathology by promoting sustained neuronal damage and dysfunction[12-15]. However, despite ongoing research, the mechanisms that connect neuroinflammation and tau pathology are still poorly understood.

Protein kinase CK2 (formerly known as Casein Kinase II), is a serine/threonine kinase that has emerged as an important regulator of neuroinflammation and protein homeostasis in several neurodegenerative diseases[16-18], and it has previously been connected to tau pathology in AD[19-22]. However, its specific role in the inflammatory pathways associated with tauopathies remains poorly defined. Interestingly, CK2 has demonstrated potential as a therapeutic target in various neurodegenerative contexts [17,18]. In AD, CK2 has been implicated in processes such as synaptic plasticity[23,24], amyloid precursor protein (APP) processing[25-27], and tau accumulation[21,22], highlighting its relevance for further investigation.

CK2 is a tetrameric enzyme composed of 2 regulatory β subunits (CK2β) and 2 catalytic subunits either α (CKα) or α' (CK2α')[16]. CK2α and CK2α' are highly similar in structure but display differential expression and substrate specificity[28-34]. CK2α is expressed throughout the body at relatively equal levels and has hundreds of substrates, while CK2α' expression is more restricted to the testes and the brain and has very few validated substrates[28-34]. Another important difference between these two catalytic subunits is the embryonic lethality of CK2α knock-out mice, while complete deletion of CK2α' does not have any major defects other than male sterility[33,34]. Recently, studies in Huntington's disease (HD) have shown the specific upregulation of CK2α' in cell and mouse models of HD as well as in affected brain tissues of patients with HD[17,18]. Importantly, HD mice lacking one allele of CK2α' showed improved synaptic function, reduced protein aggregates, and ameliorated behavioral deficits, suggesting a key role of CK2α' in this pathology[17,18].

CK2 was one of the first protein kinases identified to be altered in an AD brain[35,36], but its role in AD has been somewhat controversial due to discrepancies in the ability to detect consistent alterations in different affected tissues. Early studies using pan-CK2 antibodies (non-selective for CK2α'/CK2α subunits) showed increased levels of total CK2 in the hippocampus and frontal cortex of AD mouse models and patients with AD, especially in glial cells [37] but others have reported opposite results[35,38,39]. In those studies where levels of CK2 were elevated, the authors associated the increase in CK2 immunoreactivity with the activation of neuroinflammatory processes and AD pathology[37]. However, to date, genetic studies testing the role of CK2 (either CK2α' or CK2α) in AD/ADRD models are lacking.

Despite the lack of genetic evidence for the potential differential contribution between CK2α' and CK2α to AD pathology, several studies have proposed the role of CK2 in the phosphorylation of Tau (pTau) and tau-mediated pathology. In a kinase inhibitor screening using okadaic acid-induced pTau in Neuro-2a (N2a) cells CK2 was returned as one of the kinases whose inhibition most impacted pTau[20]. CK2 has been shown to phosphorylate the phosphatase PP2a inhibitor SET (I2PP2A/SET) increasing pTau in primary neuronal cultures treated with amyloid-β (Aβ) or overexpressing human Tau (hTau)[19]. Additionally, wild-type (WT) mice overexpressing CK2 were also shown to have increased pTau, impaired synaptic plasticity, and display cognitive deficits

like those seen in tauopathies[19]. Overall, this evidence suggests a role of CK2 in tauopathies including pTau accumulation, synaptic plasticity, and cognitive deficits.

Previous studies assessing the role of CK2 in tauopathy have largely focused on the CK2 holoenzyme without differentiating between the different catalytic CK2α and CK2α' subunits. Given the substantial difference in substrate specificity between the two catalytic subunits, it is crucial to determine whether CK2α' and CK2α contribute differently to the onset and/or progression of tauopathies. Understanding these differences is essential for designing therapeutic strategies that are both highly effective and minimize off-target effects. The lack of commercially available inhibitors that discriminate between the different catalytic subunits offers an attractive window for designing and development of specific inhibitors to selectively inhibit CK2 catalytic subunits.

Due to previous findings specifically connecting the dysregulation of CK2α' with various neurodegenerative diseases and reports linking this subunit to the phosphorylation of Tau in different contexts, we explored the role of CK2α' in various tauopathy models. We confirmed a specific upregulation at the RNA and protein levels of CK2α' in affected tissues of AD and FTD patients as well as a mouse model of tauopathy (PS19). CK2α' upregulation was specifically observed in both neurons and microglia. Importantly, genetic depletion of CK2α' in both cell and mouse models of tauopathy (expressing Tau-P301L or Tau-P301S mutations) resulted in decreased pTau. Furthermore, PS19 mice haploinsufficient for CK2α' showed improved synaptic density, synapse function, and cognition. However, the effects of CK2α' haploinsufficiency were more profoundly noted in inflammation and immune processes and in the restoration of microglia morphology, cytokine levels and phagocytic activity. Overall, our data showed a large role of the CK2α' catalytic subunit specifically in tau pathology, largely connected to the modulation of microglia functions. These studies highlight CK2α' as an attractive therapeutic target for the treatment of AD/ADRD.

Methods

Mouse Lines

For this study we used the B6;C3-Tg(Prnp-MPAT-P301S)PS19Vle/J (or PS19)[40] mouse line (Jackson #008169 maintained with purchased B6C3H breeders; obtained from Dr. Karen Ashe at University of Minnesota), and CK2α'$^{(+/-)}$ mice, originally obtained from Dr. Seldin at Boston University (Taconic biosciences TF3062)[34] and maintained on the C57Bl/6J background for several generations. We crossed PS19 and CK2α'$^{(+/-)}$ mice and this cross generated 4 genotypes of interest WT (PS19$^{0/0}$;CK2α'$^{(+/+)}$), CK2α'$^{(+/-)}$ (PS19$^{0/0}$;CK2α'$^{(+/-)}$), PS19 (PS19$^{Tg/0}$;CK2α'$^{(+/+)}$), and PS19;CK2α'$^{(+/-)}$ (PS19$^{Tg/0}$;CK2α'$^{(+/-)}$) mice. For all experiments littermate WT and CK2α'$^{(+/-)}$ controls were used. Two time points were used in experiments; pre-symptomatic (6-7 months) and symptomatic (10-12 months). All mice were housed under standard SPF conditions. All animal care and sacrifice procedures were approved by the University of Minnesota Institutional Animal Care and Use Committee (IACUC) in compliance with the National Institutes of Health guidelines for the care and use of laboratory animals under the approved animal protocol 2307-A41243.

Human postmortem tissue

Postmortem human frontal cortex (Brodmann's area 46) FTD patients and controls subjects was provided by NeuroBioBank of National Institutes of Health. A total of 6 female (3 control/3FTD) and 8 male (4 control/4 FTD) samples were used, and samples were age and sex matched. Ages ranged from 60-77 with the average age of all samples being 70. More detailed information on specific samples can be found in **supplemental table 1**.

Immunoblotting

Human and mouse protein was extracted as previously described[17]. Brain tissue was homogenized with either tissue-tearor (Biospec products, Inc) or Pellet pestle motor (Kimble Kontes) in 25 mM Tris-HCl pH 7.4, 150 mM NaCl, 1 mM EDTA, 0.1% SDS, 1% Triton X-100 and samples were incubated on ice 15-30 min and vortexed at full speed for 30 s every 5 min. Additional SDS was added to samples to bring total concentration up to 2%. Mouse protein was heated at 100°C for 5 min. Samples were centrifuged at 4°C, 13,000 g for 20 min and the supernatant was collected. Protein concentration determined using the BCA protein quantification assay (Pierce).

Immunoblotting was conducted as previously described[17]. Human and mouse protein samples were separated on 4–20% SDS Criterion TGX Stain-Free gels (BioRad) at 80 V. Proteins were transferred to a nitrocellulose membrane (BioRad 0.2 µm) in Tris–Glycine Buffer (25 nM Tris-Base, 200 mM Glycine) at 25 V for 30 min in Trans Turbo Transfer system (BioRad). The membrane was blocked with 5% non-fat dry milk in TBS containing 0.5% Tween-20 (TBST) for 1 h at room temperature. Membrane was incubated in TBST containing 2.5% milk overnight at 4 °C. The next day, membranes were incubated in secondary antibody (Amersham ECL HRP Conjugated Antibodies 1:5000) in TBST containing 2.5% milk) for 1 h at room temperature. Followed by band detection using SuperSignal Chemiluminiscent substrate (Thermo Scientific) and GE ImageQuant Las4000 mulit-mode imager. Primary antibodies and their concentrations are as follows: CK2α' (1:2000; Rabbit, Novus NB100-379) and GAPDH (1:5000; Mouse, Santa cruz sc-365062).

Cell culture: Culturing, transfections, and immunocytochemistry

Neuro-2a cells (N2a; ATCC CCL-131) were originally obtained from Dr. Veena Prahlad (University of Iowa). Cells were cultured at 37ºC 5% CO_2 in Dulbecco's modified Eagle's medium (DMEM, Genesee) supplemented with 10% fetal bovine serum (FBS), 100 U ml^{-1} penicillin/streptomycin as previously described[20,41,42]. For silencing experiments cells were simultaneously plated in 12-well plates for RNA-extraction or 24-well plates containing Matrigel matrix (Corning) coated glass coverslips for immunocytochemistry at a density of 80,000 cells/cm^2.

24 hours after plating all cells were transfected with siRNA for CK2α (Qiagen SI02007180, Rn_RGD:621663_4 FlexiTube siRNA), CK2α' (Qiagen SI00961072 Mm_Csnk2a2_4 Flexitube siRNA, Qiagen SI00961051 Mm_Csnk2a2_1 FlexiTube siRNA, Qiagen SI00961058 Mm_Csnk2a2_2 FlexiTube siRNA, and Qiagen SI00961065 Mm_Csnk2a2_3 FlexiTube siRNA pooled) or AllStars negative scrRNA control (Qiagen S103650318) using DharmaFECT 1

(Horizon discovery) at a final concentration of 25 nM in cell medium. 24 hours after siRNA transfection cells were transfected with either pEGFP-C1 plasmid (Clontech) or prk5-Tau-P301L-EGFP (Addgene #46908)[43] using jetOptimus transfection reagents (Polyplus). 24 hours after transient transfection RNA was extracted as described below and cells were fixed with 4% PFA for immunocytochemistry.

For immunocytochemistry cells were blocked in 5% NGS in TBST (0.3% triton x-100 in TBS) for 1 hour, then incubated in primary antibody diluted in overnight 5% NGS in TBST (0.3% triton x-100 in TBS) (pTau (Ser202, Thr205) AT8 (1:500; Mouse Invitrogen Mn1020)). Secondary Alexa-fluorophore-conjugated antibodies (Invitrogen) were added (1:200 in TBST with 5% NGS) for 1 h at room temperature. Coverslips were mounted in ProLong Gold Antifade with DAPI (Invitrogen) and subsequently imaged.

Immunohistochemistry

Immunohistochemistry experiments were conducted as previously described[17,44,45], and stained with either fluorescent secondaries or carried through 3,3'-diaminobenzidine (DAB) staining. Mice were anesthetized with Avertin (250 mg/kg Tribromoethanol) and perfused intracardially with tris-buffered saline (TBS) (25 mM Tris-base, 135 mM Nacl, 3 mM KCl, pH 7.6) supplemented with 7.5 mM heparin. Brains were dissected, fixed with 4% PFA in TBS at 4°C for 4–5 days, cryoprotected with 30% sucrose in TBS for 4–5 days and embedded in a 2:1 mixture of 30% sucrose in TBS:OCT (Tissue-Tek). Brains were cryo-sectioned into 16 µm-thick coronal slices and stored in a 50% glycerol-50% TBS (25 mM Tris-base, 125 mM NaCl, 3 mM KCl, pH 7.6) solution at -20ºC. For each experiment, three hippocampal containing sections were used per mouse.

For immunofluorescent staining, sections were blocked in 5% normal goat serum (NGS) in TBST for 1 h at room temperature. Primary antibodies were incubated overnight at 4°C in TBST containing 5% NGS. Secondary Alexa-fluorophore-conjugated antibodies (Invitrogen) were added (1:200 in TBST with 5% NGS) for 1 h at room temperature. Slides were mounted in ProLong Gold Antifade with DAPI (Invitrogen) and subsequently imaged. Primary antibodies used and dilutions are as follows: GFAP (1:2000; Chicken Millipore Sigma AB5541), Iba1 (1:500; Rabbit Fujifilm Wako 019-19741), Iba1 (1:500, Goat Fujifilm Wako 011-27991), NeuN (1:1000; Mouse Millipore MAB377), PSD95 (1:500; Rabbit Invitrogen 51-6900) and Vglut1 (1:500; Guinea pig Millipore AB5905). Imaging of immunofluorescent slices was conducted using a confocal microscope (Stellaris, Lecia). For NeuN, Iba1, and GFAP imaging 20x tiles were acquired with a 16um z-dimension and 1um step size. For PSD95 and VGlut1 images were acquired as described for synapse analysis.

For DAB staining antigen retrieval was performed using either Tris-EDTA pH=9.0 (Biolegend 422703) or Rodent decloaker (Biocare medical RD913) at 80ºC for 30 minutes. Sections were blocked at room temperature in TBST containing 10% NGS for 1 hour, then incubated in primary antibodies overnight at 4C in TBST containing 5% NGS. Sections were incubated in biotin-conjugated secondaries (Jackson Immuno Research Labs Biotin-SP (long spacer) AffiniPure) in TBST containing 5% NGS for 1 hour, then blocked in 3% hydrogen peroxide for 20 minutes. Sections were incubated in tertiary antibodies (VECTASTAIN Elite ABC, HRPS kit, Vector

laboratories) in TBST containing 5% NGS for 1 hour per manufacturer instructions. Sections were then incubated in DAB chromogen diluted in DAB substrate buffer (Biolegend) for sufficient staining. For counterstaining sections were incubated in 0.1% Cresyl violet for 10-12 minutes at 37ºC. Slides were then dehydrated and cleared in a series of ethanol and xylene washes before being mounted in Permount mounting medium (Fisher scientific). Primary antibodies used and dilutions are as follows: pTau (Ser202, Thr205) AT8 (1:1000; Mouse, Invitrogen Mn1020) and CD68 [RM1031] (1:2500; Rabbit, Abcam ab303565). DAB images were taken at 10x on a hybrid microscope using the brightfield settings (Echo Revolve) and at 40x on the EasyScan One slide scanner (Motic).

in situ hybridization

Tissues were collected as previously described in the immunohistochemistry procedure. Slices were mounted on superfrost plus glass slices using PBS and stored at -80ºC overnight before *in situ* hybridization. RNAscope was performed according to the ACDbio manufacturer's protocol using a custom probe for *Csnk2a2*. Immediately following RNAScope protocol, the slides were blocked with 10% Normal Goat Serum (NGS) in Co-detection antibody diluent (CDD) for 1 hour. Anti-IBA1 (Rabbit, Fujifilm Wako 019-19741) was diluted at 1:200 in 5% NGS with CDD and slides were incubated overnight. The next day secondary Alexa-fluorophore-conjugated antibodies (Invitrogen) were added (1:40 in CDD with 5% NGS) for 2h at room temperature. Slides were mounted in ProLong Gold Antifade with DAPI (Invitrogen) and subsequently imaged.

Tau pathology type

Tau pathology type analysis was conducted by 3 independent and blinded investigators. Tau pathologies were defined based on previous publications[46-49] and based on the pattern of AT8+ staining. Briefly as described by Shi et al 2017[46] type 1; displays mossy fiber and sparse and diffuse cell body staining in the dentate gyrus (DG), type 2; displays compact dense tangle like cell body staining in the DG and CA3 with some sparse CA1 cell body staining, type 3; staining is seen in the neuropil of the stratum radiatum of the CA1 staining along with staining of dendrites from pyramidal neurons and sparse cell body staining, type 4; dense fragmented, dotted, and grainy staining is observed all over the hippocampus. The percentage of pathology for the cohort for each type was determined by the following calculation; ((number of mice with pathology type)/(total number of mice in cohort)) x 100.

Image quantification

All image quantifications were conducted using either QuPath[50] or Image J (FIJI)[51] and were blinded to the experimenter. For all quantifications images names were either blinded in FIJI using the BlindAnalysis plugin or in Qupath using the automated image masking tool. Quantifications were performed with at least two blinded experimenters.

Quantification of NeuN was done automatically using QuPath cell detection. Identical ROIs were applied to each image for all 3 regions of the hippocampus. The cell detection tool was used to automatically detect NeuN+ cells based on identical thresholding settings applied to all images. Quantification of Iba1+ and GFAP+ cell counts was conducted as we previously described[44,45].

An average projection of 20x tiled z-stack confocal image was generated in FIJI and used for counting. Two consistent ROIs (~3900 um^2) were drawn within the CA1, CA3, and DG for counts and the cell counter FIJI plugin was used to count cells manually. A cell was determined to be Iba1+ or GFAP+ based on the presence of DAPI within the stained area. Results were averaged and normalized per mm^2 and reported as animal averages (2 ROIs/slice; 3 slices/animal). Quantification of DAB positive percent area was quantified using either the Colordevonvolution2 plugin in FIJI[52] or in QuPath. Briefly a threshold of positive DAB staining was determined and applied to all images to then calculate the percentage positive area.

Quantification of PSD95+ puncta within Iba1+ microglia were performed using Imaris software (Bitplane). A confocal microscope (Stellaris, Lecia) was used to acquire images in the CA1 stratum radiatum region of the hippocampus with a 40x objective and 3x zoom factor with 0.34 size z-steps for a total of 15 steps. Lecia Stellaris software lighting processing was applied before analysis. Images were then 3D rendered in Imaris and cropped to isolate individual Iba1+ cells (2 per slice). Iba1+ surfaces were generated and used to mask PSD95+ signal. The masked PSD95+ signal was then used to create spots, to ensure it was located within Iba1+ signal. The number of spots within the Iba1+ surfaces per cell soma defined as the region where Iba1+ signal colocalized with DAPI and within the whole Iba1+ cell surface were counted and reported as a number.

Synapse analysis

Synapse analysis was conducted as previously described[17,45,53-55]. Immunohistochemical staining was conducted as described above with Vglut1 and PSD95, with blocking increased to 20% NGS+TBST for 2 hours and primary and secondary antibodies diluted in 10% NGS+TBST. Fluorescent images from the molecular layer of the CA1 were taken on a confocal microscope (Stellaris, Lecia) at 63x with z-step dimension of 0.34 µm with 15 steps were generated. Lecia stellaris software lightning processing was applied to images post-acquisition and edited images were used for analysis. Maximum projections of three sections per slice were generated. Puncta analyses were conducted blinded using the PunctaAnalyzer Plugin (Durham,NC,USA) in FIJI as previously described[17,45,53-55]. Data is represented as slice averages with three slices per animal.

Electrophysiology

Mice were anesthetized with isoflurane (2%) and decapitated for slice preparation. After decapitation, the whole brain, containing the two hippocampi, was removed into ice-cold solution consisting of: sucrose 189 mM, glucose 10 mM, NaHCO3 26 mM, KCl 3 mM, MgSO4 5 mM, CaCl2 0.1 mM, NaH2PO4 1.25 mM. Brains were positioned on the stage of a vibratome slicer and cut to obtain transverse hippocampal slices (350 µm thick; LEICA VT1000S). Slices were incubated at room temperature in artificial cerebrospinal fluid (aCSF) continuously oxygenated for 45 min-1 h before use. aCSF contained NaCl 124 mM, KCl 5 mM, NaH2PO4 1.25 mM, MgSO4 2 mM, NaHCO3 26 mM, CaCl2 2 mM, glucose 10 mM; gassed with 95% O2, 5% CO2. The pH was adjusted to 7.4 with NaOH. All experiments were carried out at 30–34°C, during which the slices were continuously perfused with solution.
Field excitatory postsynaptic potentials (fEPSPs) were recorded in the CA1 region of the hippocampus. fEPSPs in the CA1 region of the hippocampus were evoked with a stimulating electrode placed on the Schaffer collateral (0.33 Hz) using brief current pulses (200 µs, 0.1–0.2

mA). Extracellular recording electrodes were filled with aCSF. Stimulation was adjusted to obtain a fEPSP peak amplitude of approximately 1 mV during control conditions. After a stable fEPSP baseline period of 10 min, LTP was induced by a Theta-burst stimulation (TBS) consisting of a series of 10 bursts of 5 stimuli (100 Hz within the burst, 200 ms interburst interval), which was repeated 4 times (5 s apart). Data were filtered at 3 kHz and acquired at 10 kHz using pCLAMP 10.2 software (Molecular Devices, RRID: SCR_011323).
A stimulus-response curve (0.05-0.4 mV, mean of five fEPSPs at each stimulation strength) was compiled for the different mice used. For paired-pulse ratio experiments, two fEPSPs were evoked 40 ms apart for 0.5 min at baseline frequency (6 times) at the beginning of the baseline recording. The PPR was expressed as the amplitude of the second fEPSP divided by the amplitude of the first fEPSP.

Behavior

Behavioral testing was performed with the support and guidance of the Mouse Behavior Core at University of Minnesota. Mice were handled daily for a minimum of one week prior to all behavioral testing. Mice were habituated to behavior room for a minimum of 30 minutes each day prior to beginning of task. All tasks were recorded and tracked using ANYmaze software (Stoelting Co., Wood Dale, Illinois) and overhead cameras.

Barnes maze was conducted on a 20 hole Barnes Maze (San Diego Instruments) divided into 4 quadrants and a center zone under 450-500lux light intensity, with black and white visual cues placed around the room, as similarly described[56-58]. Mice were placed in the center under a covering with lights off, lights were turned on and covering lifted within 30 seconds. The training phase consisted of four 3-minute trials per mouse for 5 days, with an inter trial interval of approximately 20-30 minutes. The maze was thoroughly cleaned with 70% between all mice and rotated between trials to avoid olfactory cues. Mice were allowed to explore the maze and primary latency, or the time to first explore the escape hole, was recorded. The trial either concluded when the mouse entered the escape hole, or at 3 minutes at which point the mouse was gently guided to the escape box. For the probe day the escape hole was covered with an identical covering used on all other holes, mouse was placed on the maze in the same manner as training. The time spent in each maze zone was then recorded. Spatial strategy was determined by a blinded investigator.

Open field was conducted in 40cmx40cm boxes with a 150-200lux overhead light. Mice were placed in boxes and behavior was recorded for 1 hour. Boxes were thoroughly cleaned between mice with 70% ethanol.

RNA extraction and qPCR

RNA was extracted from cells and mouse striatal tissues by using the RNeasy extraction kit (Qiagen) according to the manufacturer’s instructions. cDNA was prepared using the Superscript First Strand Synthesis System (Invitrogen). SYBR green based PCR was performed with SYBR mix (Roche). The qPCR amplification was performed using the LightCycler 480 System (Roche). Each sample was tested in triplicate and normalized to GAPDH levels.

For qPCR the following primers were used: CK2α' **FWD-**CGACTGATTGATTGGGGTCT **REV-**AGAATGGCTCCTTTCGGAAT; CK2α **FWD-**TCCCCATGCTGTGACAATAA **REV-**AAGACCCTGTGTCACGAACC; CK2β **FWD-** AGTCCTCCAGACACCACCAC **REV-**GACTGGGCTCTTGAAGTTGC; huTau **FWD-** GCTGGCCTGAAAGCTGAAGA **REV-**CGTTTTACCATCAGCCCCCT.

RNA-Seq Analysis

RNA was extracted as previously described and RNA-Sequencing was conducted by Novogene (Sacramento, CA). Gene expression analysis was carried out using the CHURP pipeline (https://doi-org.ezp2.lib.umn.edu/10.1145/3332186.3333156) using n=4-7 mice/genotype with female(F)/male(M) ratios as follows; 4 WT (2F/2M), 5 CK2α'$^{(+/-)}$ (2F/3M), PS19 (3F/4M) (3 high pathology and 4 low pathology), and 4 PS19;CK2α'$^{(+/-)}$ (3F/1M). Differential gene expression was determined with DESeq2 using default setting[59] (v1.46.0). Genes with a FDR <= 0.05 were considered significant. Outliers' identification was performed using Cook's distance (DESeq2). Driver factors of gene expression variance (genotype and/or sex) were evaluated using R (v4.4.2) package variancePartition (1.36.3). Pathway and clustering analysis were completed gProfiler2[60] (v0.2.3) and clusterProfiler (v4.14.6). Data visualization was done using various R graphic packages, including ggplot2, ggraph, and DESeq2 visualization functions. The RNA-seq data set generated in this manuscript has been deposited at GEO (accession number GSE298505).

Microglia morphology

Microglia morphology measurements were adopted from previously described protocols[61]. Slices were stained with Iba1+ as described in the immunohistochemistry methods. Nine total cells were imaged per animal across 3 slices with 3 cells per slice. Images were taken on a confocal microscope (Stellaris, Lecia) at 40x magnification with a zoom factor of 2.5. Z-stacks were acquired with a Z-step size of 0.3 µm, covering the entire slice. Maximum projection of z-stacks were generated via FIJI for analysis. For image analysis, brightness and contrast were adjusted to subtract background noise before converting the image into a binary black-and-white version of the original. The paintbrush and despeckle functions were used to remove any additional noise before applying the skeletonizing function. Finally, the AnalyzeSkeleton plugin[62] was used to quantify the resulting skeleton image.

Cytokine proteome profiling

The Proteome Profiler Mouse Cytokine Array Panel (ARY006, R&D Systems) was used to detect the levels of cytokine/chemokine as per manufacturer's instructions. Frozen hippocampi from 9 months old PS19 and PS19;CK2α'$^{(+/-)}$ mice were homogenized in PBS containing Halt protease inhibitor cocktail and phosphatase inhibitors (Fisher Scientific) and 1% triton X-100 (Sigma). Samples were stored at -80°C for 15 min, thawed and centrifuged at 10,000 × g for 5 min to remove cell debris. 300 µg of protein was applied to each membrane and the manufacturer's protocol was followed. A total of n=4 mice/genotype with a female(F)/male(M) ratio (2F/2M PS19 and 2F/2M PS19;CK2α'$^{(+/-)}$) were analyzed. Imaging was conducted as described for immunoblotting. Spot intensity was quantified using FIJI software and a batch

correction was applied to normalize data. Membrane spots corresponding to 40 different cytokines or chemokines were measured as outlined in manufacturer protocol.

Statistical analyses and data representation

For electrophysiology experiments data were analyzed using Clampfit 10.2 software (pCLAMP, Molecular Devices, RRID: SCR_011323). Data are presented as mean ± SEM. To estimate changes in synaptic efficacy, STP was quantified by comparing the mean fEPSP amplitude during 1 minute after the application of the TBS. LTP was quantified as for STP but 40 minutes after the protocol. Graphs were obtained using SigmaPlot 14.0. Before applying any statistical comparison, the data were subjected to Shapiro- Wilk normality and equal variance tests. For any comparisons between two groups, two- paired Student's t-test was used. For multiple comparisons to the same control, one- way ANOVA and Holm-Sidak test was used. P-values less than 0.05 were considered statistically significant.

For all other experiments GraphPad Prism (GraphPad, San Diego, CA, USA) was used to create graphs and conduct statical testing. For all other experiments data is represented as mean ± SEM. Statistical analyses were performed using paired Student's t-test, unpaired student's t-test, one-way or two-way ANOVA with post-hoc analysis, as indicated in each figure legend. A p-value <0.05 was considered significant.

Results

Levels of Protein kinase CK2α' are increased in the brains of dementia patients and mouse models of tauopathy

There are two different genes (*Csnk2a1* and *Csnk2a2*) that code for two different CK2 catalytic subunits CK2α and CK2α', respectively. These two catalytic subunits share a high percent of homology and they can arrange in various combinations (α-α, α-α' or α'-α') depending on their expression and tissue availability although the canonical arrangement in the brain is expected to be α-α' (**Fig. 1A, B**)[16,28-34]. To determine whether CK2 catalytic subunits are altered in patients with dementia we utilized the RNA-seq data from the Allen Brain Institute: Aging, Dementia, and Traumatic Brain Injury (TBI) Study. In this dataset, three different regions were available: parietal cortex (PCx), temporal cortex (TCx) and hippocampus (HIP). Analyzing this dataset [63] we found a specific increase in the expression of *CSNK2a2,* encoding for CK2α', but not in *CSNK2a1*, encoding for CK2α, in patients with dementia compared to non-dementia controls in the PCx (**Fig. 1C-F**). We also found a trend towards increased CK2α' in the TCx and HIP although data did not reach statistical significance (**Fig. 1C, G, H**). Importantly, we also observed a significant increase in CK2α' protein levels in the frontal cortex of FTD patients compared to age and sex-match controls (**Fig.1I, J, Supp. Table 1**). Enhanced levels of CK2α' also associated with the presence of tau pathology previously assessed in those samples using the AT8 antibody (**Fig. 1K, Supp. Table 1**). The majority of FTD samples grouped in the top left quadrant representing high levels of CK2α' and the presence of tau pathology, while most control samples grouped in the bottom right quadrant representing low levels of CK2α' and

absence of tau pathology. For those two control samples (#1 and #6) in which tau pathology was observed, the AT8 phospho-tau (pTau) signal and distribution differed from the canonical tau pathology associated with dementia and individuals lacked classical cognitive decline (**Supp. Table 1**).

To examine whether CK2α' was also elevated in mouse models of tauopathy we utilized the PS19 mouse model, which expresses human tau with a P301S mutation associated with familial forms of FTD and other tauopathies[40]. Pathology and neuronal loss in PS19 mice are seen largely in the hippocampus, although it does spread to other brain regions including the neocortex, entorhinal cortex and amygdala[40,64]. We conducted RNA in situ hybridization for CK2α' in the hippocampus of PS19 mice at a symptomatic age (10-12 months), defined as the age at which animals present overt tau pathology and cognitive decline[40,65,66]. We observed a significant increase in CK2α' in all regions of the hippocampus specially in the pyramidal and granular layers, that colocalized with NeuN staining, pointing to enhanced expression in neurons (**Fig. 2A-D**). Expression outside the neuronal layer was also observed which associated with enhanced CK2α' levels in the microglia (Iba1+) of PS19 mice compared to WT (**Fig. 2E-G**). Single cell RNA-Seq studies available in The Alzheimer's Cell Atlas (TACA)[67-71] confirmed increased CSNK2a2 expression in patients with AD in both microglia and neurons in the occipital cortex (OL) and entorhinal cortex (EC) respectively (**Supp. Fig. 1**). However, studies in prefrontal cortex (PFC) and frontal lobes (SFG) revealed enhanced expression of CSNK2a2 in cells other than neurons and microglia, suggesting a cell-specific upregulation of CSNK2a2 that seems to be brain region-dependent. Overall, these results demonstrate a specific upregulation of CK2α' in brain affected regions of patients with dementia and in hippocampal neurons and microglia of mouse models of tauopathy.

Genetic depletion of Protein kinase CK2α' impacts tau pathology *in vitro* and *in vivo*

Previous studies have shown that CK2 holoenzyme regulates tau phosphorylation in various cell and mouse models of AD[19,72], but whether CK2α' subunit specifically contributes to this phenomenon is unknown. To explore whether CK2α' has any role in the regulation of tau phosphorylation and pathology we first explored the impact of silencing CK2α or CK2α' in Neuro2a (N2a) cells expressing a pathological tau variant (Tau-P301L). N2a cells were treated with either scrambled RNA (ScrRNA) or silencing RNA for CK2α (siCK2α) or CK2α' (siCK2α'), and transfected with either Tau-P301L-EGFP[43] or EGFP empty vector (control) (**Fig. 3A**). The AT8 phospho-tau (pTau) antibody was then used to examine the impact of silencing CK2α and CK2α' on tau pathology (**Fig. 3B**). First, we confirmed the efficacy of the siRNAs decreasing the expression of CK2α or CK2α' without altering the other subunits (**Fig. 3C-E**) and the increased expression of Tau in N2A transfected cells (**Fig. 3F**). As expected, the levels of AT8 increased upon expression of Tau-P301L in N2A control cells (**Fig. 3B, G**). Importantly, AT8 levels decreased in Tau-P301L transfected cells treated with siCK2α' ($p=0.0130$) but not siCK2α relative to Tau-P301L ScrRNA condition ($p=0.9722$) (**Fig. 3B, G**). Our data demonstrates an impact of the CK2α' subunit specifically on pTau accumulation *in vitro* (**Fig. 3H**).

We then generated a PS19 mouse haploinsufficient for CK2α' (PS19;CK2α'$^{(+/-)}$)(**Supp. Fig. 2A-F**), to assess the impact of depleting CK2α' on survival, tau pathology and symptomatology *in vivo*. We then assessed tau phosphorylation in the hippocampus and overlaying cortex of mice

at a prodromal stage (~7 moths) and at a late symptomatic age (~10-12 moths)[40] (**Fig. 4A-B, Supp. Fig. 3A-B**). In the prodromal age no significant differences were observed in the accumulation of AT8 in PS19 and PS19;CK2α'$^{(+/-)}$ in all three examined regions of the hippocampus (CA1, CA3, and DG) and overlaying cortex (**Fig. 4C-E, Supp Fig. 3C**). As expected, in the late symptomatic groups we observed a significant increase in AT8+ area in both the PS19 and PS19;CK2α'$^{(+/-)}$ mice in the CA1, CA3, and DG and cortex relative to all other groups (**Fig. 4C-E, Supp. Fig. 3C**). However, PS19;CK2α'$^{(+/-)}$ mice showed a significant decrease in AT8 signal compared to PS19 in the CA1, DG, and cortex (CA1; $p=0.0075$, DG; $p=0.0186$ and Cortex; $p<0.0001$) (**Fig. 4C,E, Supp. Fig. 3C**) suggesting an overall decrease in pTau upon depletion of CK2α'.

Tau pathology has been previously reported to follow a characteristic progressive pattern of deposition in the hippocampus that can be categorized into 4 pathology types[46-49] (**Fig. 4F**). These pathology types have been shown to correlate with hippocampal volume[46,49] and offer a more holistic pathological assessment. We observed differential distributions of patterns between PS19 and PS19;CK2α'$^{(+/-)}$ mice with a more dramatic alteration in late symptomatic stages where nearly all PS19 mice presented a type 4 pathology in contrast to the PS19;CK2α'$^{(+/-)}$ that presented a variation in types with almost 50% of mice presenting type 2 pathology (prodromal $p=0.11$, and symptomatic $p=0.0587$) (**Fig. 4G**).

Interestingly, although CK2α' seemed to play a clear role in modifying the progression of tau pathology in PS19 mice, no significant differences in survival were observed between PS19 and PS19;CK2α'(+/-) animals, with both groups showing approximately 50% mortality by 50 weeks of age (**Supp. Fig. 2G**). Survival is a relatively coarse endpoint, influenced by the dysfunction of multiple neural and systemic pathways like the spinal cord and brain stem[40,73]. While CK2α' depletion clearly impacted tau phosphorylation and tau burden in the hippocampus and cortex, these effects were insufficient to alter the overall lifespan of this aggressive model. Nonetheless, the observed modulation of tau pathology underscored a critical role for CK2α' in specific aspects of tau-mediated neurodegeneration. We therefore decided to further explore the molecular and cellular changes influenced by CK2α' modulation in PS19 mice.

CK2α' happloinsufficiency improved hippocampal synaptic density and synaptic function in PS19 mice

We conducted NeuN immunostaining analyses in the hippocampus of PS19 and PS19;CK2α'$^{(+/-)}$ mice to determine if depletion of CK2α' could impact the overall neuronal loss characteristic of PS19 mice[40,74-76]. Significant depletion of NeuN+ cells and hippocampal atrophy was only seen in PS19 groups at a symptomatic age (**Fig. 5A, B, Supp. Fig. 4A-C**). An ~30-50% reduction in the number of NeuN counts is often reported at late symptomatic ages in PS19 mice[40,74-76]. However, we noticed a great variability in the number of NeuN+ cells and hippocampal area among PS19 littermates at this disease stage that was not related to sex (**Supp. Fig. 4D-F**). Wide variability in tau pathology and neuronal degeneration within this mouse model has been previously reported and associated to nuances in the genetics of this model[77]. Therefore, we categorized PS19 and PS19;CK2α'$^{(+/-)}$ animals presenting NeuN counts within 10% of the WT as

"abnormally low pathology" and as a result 3 PS19 animals and 1 PS19;CK2α'$^{(+/-)}$ were excluded from subsequent analyses. Analyses in curated groups of PS19 and PS19;CK2α'$^{(+/-)}$ mice revealed a significant increase in the number of NeuN+ cells in PS19;CK2α'$^{(+/-)}$ mice compared to PS19 in the CA1 (**Fig. 5A, B, Supp. Fig. 4A-C**).

We then evaluated if total synapse density was also positively altered in the CA1. We conducted immunostaining and colocalization analyses for the vesicular glutamate transporter 1 (VGlut1) (pre-synaptic marker of excitatory synapses), and the postsynaptic density protein 95 (PSD95) (post-synaptic marker) (**Fig. 5C-I**). As expected, PS19 mice showed a significant decrease in the number of synapses (colocalized puncta VGlut1-PSD95) compared to WT mice (**Fig. 5F, I**). The reduction in colocalized puncta in PS19 mice was due to a concomitant reduction in both PSD95 and VGlut1 markers (**Fig. 5D, E, G, H**). In PS19;CK2α'$^{(+/-)}$ mice we found that although there is not a statistical significance compared to PS19 mice, CK2α' haploinsufficiency decreased the % loss of both PSD95 (**Fig. 5D, G**) and VGlut1 (**Fig. 5E, H**). This resulted in the amelioration of total synapse loss in PS19;CK2α'$^{(+/-)}$ mice and obtained values for colocalization were no longer significant respect to WT (**Fig. 5F, I**). These results demonstrate a partial rescue in the density of excitatory synapses in the CA1 of PS19;CK2α'$^{(+/-)}$ mice aligning with the amelioration of hippocampal atrophy observed in this region (**Fig. 5B**).

To investigate functional implications of the rescue seen in CA1 hippocampal atrophy and synaptic density we assessed hippocampal synaptic plasticity by performing extracellular field excitatory postsynaptic potential (fEPSP) recordings in the CA1 region of acute hippocampal slices (**Fig. 5J, K**). Theta-burst stimulation (TBS) at the Schaffer collaterals induced short-term potentiation (STP), which resulted in a significant increase in synaptic efficacy at CA1 synapses in both WT and CK2α'$^{(+/-)}$ mice, as evidenced by the enhanced fEPSP amplitude (170 ±13%, n = 6; 170 ± 12%, n = 7) (**Fig. 5L, M**). In contrast, the increase in fEPSP amplitude was significantly reduced in PS19 and PS19;CK2α'$^{(+/-)}$ mice relative to WT controls post TBS (123 ± 4%, n = 7; 128 ± 7%,n = 6; **Fig. 5L, M**), indicating impaired STP in these models. Furthermore, we examined long-term potentiation (LTP) at CA3-CA1 synapses, a form of synaptic plasticity linked to learning and memory. It has been previously shown that PS19 mice present impaired LTP in the CA1-CA3 pathway[40,78,79]. First, we observed significant differences in input-output curves at CA3-CA1 synapses between PS19 and PS19;CK2α'$^{(+/-)}$ mice when compared to WT, which suggests that excitatory synaptic input properties were altered in these models (**Fig. 5N**). TBS at the Schaffer collaterals induced robust LTP in both WT (173 ± 12%, n = 6) and CK2α'$^{(+/-)}$ (164 ± 9%, n = 7; **Fig. 5L, O**). However, in the PS19 mouse model, the magnitude of LTP was significantly diminished compared to WT (128 ± 9%, n = 7; vs. WT p=0.007) (**Fig. 5L, O**), suggesting a disruption in the molecular mechanisms underlying LTP. Interestingly, in the PS19;CK2α'$^{(+/-)}$ mice, LTP was partially restored (150 ± 6%, n = 6; vs. WT p=0.199) (**Fig. 5L, O**), pointing to a potential compensatory mechanism that partially mitigates the LTP deficits observed in the PS19 mice. Importantly, paired-pulse facilitation (PPF) was unaltered across all experimental groups, suggesting that the observed changes in synaptic plasticity were most likely due to postsynaptic mechanisms dependent on the hippocampus (**Supp**. **Fig. 5**).

CK2α' haploinsufficiency improved PS19 behavior on Barnes Maze

We then tested whether the partial rescue observed in PS19;CK2α'$^{(+/-)}$ mice associated to synaptic density and functional LTP along with the decrease in Tau pathology had any impact in cognitive behaviors. Mice were trained on the Barnes maze task for 5 consecutive days on the location of a target hole (training) and on the 6th day a probe trial was conducted with the target hole removed (**Fig. 6A**). During the training trials the primary latency or the time to first locate the escape hole was recorded (**Fig. 6B-C**). All mice in the prodromal group demonstrated an improvement on time needed to locate the escape hole from day 1 vs day 5 (WT p=0.0272; PS19 p=0.0.0067; CK2α'$^{(+/-)}$ p=0.0002; PS19;CK2α'$^{(+/-)}$ p<0.0001) with no significant difference between the genotypes (**Fig. 6B**). All mice in the symptomatic group also showed a capability of acquiring the task demonstrating a significant improvement from day 1 vs day 5 (WT p<0.0001; PS19 p=0.0109; CK2α'$^{(+/-)}$ p<0.0001; PS19;CK2α'$^{(+/-)}$ p=0.0037). However, PS19 and PS19;CK2α'$^{(+/-)}$ showed a significant impairment compared to WT, starting on day 3 for PS19 (p=0.0009) and day 4 for PS19;CK2α'$^{(+/-)}$ (p=0.0306) (**Fig. 6C**). The training data suggested that both symptomatic PS19 and PS19;CK2α'$^{(+/-)}$ mice showed similar impaired learning on the Barnes Maze compared to WT mice, although deficits in PS19;CK2α'$^{(+/-)}$ were attenuated.

Following the training phase of the Barnes maze we conducted a probe phase in which the escape hole was covered and the time spent exploring the escape hole quadrant was recorded. At the prodromal age there was no significant difference in time spent in the escape hole quadrant for any genotype (**Fig. 6D**). At the symptomatic age, the PS19 mice showed a significant impairment in the time spent in the goal quadrant compared to WT (p<0.0001) (**Fig. 6D**). Importantly, the PS19;CK2α'$^{(+/-)}$ mice spent significantly more time than the PS19 mice in the goal quadrant with no significant difference from WT (vs. PS19 p=0.0113 vs. WT p=0.2335) demonstrating a rescue in spatial memory for the PS19;CK2α'$^{(+/-)}$ on the probe phase of the Barnes maze (**Fig. 6D**).

The PS19 mouse model is known to present motor deficits due to hindlimb paralysis and weakness[40], which could confound Barnes Maze results if PS19 mice perform more poorly due to less distance traveled. Prodromal mice displayed no difference in distance traveled on Barnes Maze (**Supp. Fig. 6A**). While the symptomatic PS19 mice traveled less distance in the Barnes Maze compared to WT mice, they did not show a significant difference in distance traveled compared to PS19;CK2α'$^{(+/-)}$ mice (**Supp Fig. 6B**). In addition, in open-field testing we found no differences between groups at the prodromal time point (**Supp. Fig. 6C**). On the contrary, symptomatic mice showed significant hyperactivity in the open field task, demonstrating the ability of PS19 mice to move (**Supp Fig. 6D**). Indeed, no significant differences were observed in the open field between PS19 and PS19;CK2α'$^{(+/-)}$ mice (**Supp Fig. 6D**). This data supports the improvement in cognitive abilities seen in the PS19;CK2α'$^{(+/-)}$ mice are not due to changes in motor function but rather are related to an improvement in memory.

Mice can use different cognitive strategies to navigate the Barnes Maze and locate the escape hole[57]. As the mouse learns the task they show improvement in the strategy used to locate the escape hole[57] (**Fig. 6E**). Assessing these cognitive strategies is important to provide a deeper insight into how memory and spatial learning are being utilized. All animals in the prodromal group demonstrated a similar pattern in spatial strategies over the training phase (**Fig. 6F**) and showed a predominance in the corrected and direct strategies in the probe phase (**Fig. 6G**).

Symptomatic PS19 and PS19;CK2α'$^{(+/-)}$ mice both showed impaired spatial strategies over the training phase, by day 5 both genotypes largely displayed either failing, random or serial strategies (**Fig. 6H**). However, during the shortened probe phase, PS19 displayed a worsened overall strategy, with predominant failing, serial, and long correction strategies compared to PS19;CK2α'$^{(+/-)}$ mice that displayed more serial, corrected and direct strategies (**Fig. 6I**). Overall, the PS19;CK2α'$^{(+/-)}$ mice displayed improvement in the probe phase of the Barnes Maze in both the time spent in the escape quadrant and strategy used to locate the target, indicating improvements in spatial memory.

RNA-Seq analyses revealed CK2α' alters the expression of genes related to immune response and synaptic function

To start interrogating the mechanisms by which CK2α' influences tau pathology and cognitive decline in PS19 mice we conducted RNA-Seq analysis in the hippocampus of animals in the prodromal phase. The reason we focused on this particular age group is because the prodromal phase represents the initial stage of disease development that precedes overt symptoms. During this time, sometimes subtle but significant molecular changes begin to occur, including alterations in gene expression that precede the onset of full-blown pathology. By focusing on this phase, we aimed to identify pathways involved in disease onset that may be missed if only later stages of the disease are studied where significant neuronal loss is present. Our RNA-seq analyses revealed a large variability in the expression pattern of PS19 mice that associated to the variability observed in NeuN counts (**Supp. Fig. 4D-F**). By comparing the expression pattern of the different animals along with the tau pathology we found two distinct expression profiles that allowed the mice to segregate into a low (Low-PS19) and high (High-PS19) pathology groups (**Supp. Fig. 7A**). These two different pathology groups showed differential gene expression compared with WT from one another (**Supp. Fig. 7B-C**). With the Low-PS19 group primarily differentially dysregulated genes (DGEs) related to developmental and organizational pathways (**Supp. Fig. 7B**) and the High-PS19 showing DGEs related to immune processes (**Supp. Fig. 7C**). Interestingly, the High-PS19 group was more similar in the gene expression pattern to the PS19;CK2α'$^{(+/-)}$ group than the Low-PS19 group (**Supp. Fig. 7D-E**). Moreover, the PS19;CK2α'$^{(+/-)}$ mice showed a more similar expression pattern among animals of the same group. Moving forward we focused our comparisons on the High-PS19 group with PS19;CK2α'$^{(+/-)}$.

Gene expression analyses in the High-PS19 cohort (referred hereafter as PS19) vs WT mice identified 477 significant DGEs in the PS19 vs WT (**Fig. 7A**). Gene ontology pathway analysis revealed that many of the DGEs belonging to the top dysregulated pathways corresponded to immune and inflammatory functions (**Fig. 7B**), as previously reported[80,81]. Other important GO pathways were associated with synaptic dysfunction where the top 5 impacted synaptic pathways in PS19 mice corresponded to dysregulation in synapse assembly, regulation of synapse organization, regulation of synapse structure or activity, post synapse organization and synaptic pruning (**Fig. 7B-C**). Synaptic pruning was upregulated in PS19 vs WT, whereas the other synaptic pathways related to organization and regulation of activity were largely downregulated (**Fig. 7C**). These results aligned with the decreased synapse density and

impaired synaptic function seen in PS19 mice and indicated a potential early prodromal transcriptional signature for these deficits.

Direct comparison of PS19 vs PS19;CK2α'$^{(+/-)}$ mice yield a small set of 26 significant DGEs (**Fig. 7D**). This small gene set returned no biologically connected pathways via gene ontology analysis, but several of the DGEs were related to Apoptotic/phagocytic and Immune/inflammatory functions (*Cept1, Ube2n, Oxct1, Exoc3, Adgrb1, Sh3glb2*, *Adgrdb1*). We then assessed whether the manipulation of CK2α' had any overall effect on modules of genes with similar biological functions despite not reaching the >Log2 criteria. Weighted Gene Co-Expression Network Analysis (WGNCA) revealed 34 gene modules with 8 modules (red, lightcyan, royalblue, skyblue, tan, lightyellow, turquoise, and black) showing statistical significance detected via a Kruskal-Wallis test among our groups ($p<0.05$) (**Fig. 7E,F, Supp. Table 2**). Interestingly several of these modules (red, tan, and black) showed a trend where the PS19;CK2α'$^{(+/-)}$ mice more closely resembled the expression pattern of WT mice. On the contrary, other modules showed a larger dysregulation in the PS19;CK2α'$^{(+/-)}$ compared to WT and PS19, such as the lightcyan, lightyellow, and turquoise. Among the 8 significant gene modules, we focused our analyses on the tan and turquoise modules for showing a different expression pattern between PS19 and PS19;CK2α'$^{(+/-)}$ mice. The tan module composed on 215 genes (Kruskal-wallis $p=0.016$) (**Fig. 7F-G, Supp. Fig. 8A, Supp. Table 2**) was represented by pathways associated with synaptic function and assembly, with top pathways being vesicle-mediated transport in synapse, synaptic vesicle cycle, and regulation of synapse organization (**Fig. 8G**). The overall expression of genes associated with these pathways presented a depletion in the PS19 mice that was ameliorated in the PS19;CK2α'$^{(+/-)}$ group (**Fig. 7F**). Changes in these pathways aligned with the improvements observed in NeuN abundance, synapse density and function in PS19;CK2α'$^{(+/-)}$ mice (**Fig. 5**).

On the other hand, the turquoise module composed of 2765 genes (Kruskal-wallis $p=0.0041$) displayed a dysregulation in the same direction in both PS19 and PS19;CK2α'$^{(+/-)}$ mice, with a greater dysregulation in PS19;CK2α'$^{(+/-)}$ (**Fig. 7F,H, Supp. Fig. 8B, Supp. Table 2**). This module was a large collection of genes including top significant pathways related to innate immune response and immune response-activating signaling pathways (**Fig. 7H**). PS19;CK2α'$^{(+/-)}$ mice showed a higher expression than PS19 of a large set genes associated with immune response perhaps indicating an improved activation of immune systems.

To further explore DGEs specific to the PS19 and PS19;CK2α'$^{(+/-)}$ mice we focused specifically on their comparisons to WT. We set criteria to yield two comparisons (*comparison 1*) significant DGEs in PS19 vs WT but not PS19;CK2α'$^{(+/-)}$ vs WT and (*comparison 2*) significant DGEs in PS19;CK2α'$^{(+/-)}$ vs WT but not PS19 vs WT. This more restrictive criteria then yielded two unique set of genes (**Supp. Table 3**). Biological pathways associated with *comparison 1* included regulation of neurogenesis, positive regulation of nervous system development and regulation of synapse organization (**Supp. Fig. 8C**), similar to those pathways identified in the tan module. Biological pathways associated with *comparison 2* included those associated with inflammatory or immune responses (**Supp**. **Fig. 8D**). The majority of genes included in the top two biological pathways were upregulated in PS19;CK2α'$^{(+/-)}$ mice and associated with immune response (**Supp. Fig. 8D, E**). These results indicate there are more immune-related genes significantly

differentially expressed in the PS19;CK2α'$^{(+/-)}$ compared to WT than PS19 compared to WT similar to what was revealed in the turquoise module (**Fig. 7H**). This was also confirmed by gene set variation analysis (GSVA) activity scores of the dysregulated pathways within *comparison 2* showing increased activity of pathways associated with immune response relative to WT (**Fig. 7I**). This analysis also revealed interesting alterations in apoptotic pathways. We observed a decrease in activity in extrinsic apoptotic pathways and an increase in intrinsic apoptotic pathways in the PS19;CK2α'$^{(+/-)}$ when comparing to PS19 mice (**Fig. 7I**). This suggests a shift in the molecular mechanisms governing the apoptotic pathway towards a more beneficial and selective apoptotic environment perhaps contributing to the beneficial outcomes observed in PS19;CK2α'$^{(+/-)}$ mice. Overall, the RNA-Seq analyses revealed that CK2α' haploinsufficiency caused alterations in networks of genes associated with important and relevant biological pathways demonstrating the amelioration of synaptic dysfunction, the enhanced activation of immune related pathways, and impacts on apoptotic signaling.

PS19 mice lacking CK2α' ameliorated microglia reactivity, neuroinflammation and phagocytic activity

Considering the enhanced levels of CK2α' in microglia, the activation of pathways involved in immune response upon deletion of CK2α', and the key role of microglia as CNS immune cells in tauopathies and dementia[12,40,82-85], we examined the state of glial cells (astrocytes and microglia) in the hippocampus in both the prodromal and symptomatic mice groups. First, we observed a significant increase in the number of GFAP+ cells in the hippocampus of PS19 mice in both age groups (**Supp. Fig. 9A-E**), as previously reported[40], but we did not find any differences compared to PS19;CK2α'$^{(+/-)}$ mice (**Supp. Fig. 9C-E**). However, GFAP+ cells significantly decreased in the PS19;CK2α'$^{(+/-)}$ compared to the PS19 mice in the overlaying cortex of symptomatic mice (**Supp. Fig. 9F-H**). When looking at Iba1+ cells we observed a modest but significant increase in Iba1+ positive cells throughout the hippocampus in the prodromal PS19 mice compared to WT (**Supp. Fig. 10A,C-E**). In the symptomatic group, both the PS19 and PS19;CK2α'$^{(+/-)}$ demonstrated a much greater increase in the number of Iba1+ cells compared to WT, but PS19;CK2α'$^{(+/-)}$ mice presented significantly less Iba1+ cells than PS19 in both the CA1 (**Fig. 8A,B, Supp. Fig. 10B, C**) and CA3 (**Supp. Fig. 10B,E**). No significant differences were observed among the PS19 gin the DG (**Supp. Fig. 10B, E**). We also observed significantly less Iba1+ cells in the PS19;CK2α'$^{(+/-)}$ compared to PS19 mice in the overlaying cortex of symptomatic mice (**Supp. Fig. 10F-H**).

We also examined microglia morphology using measurements corresponding to ramification and correlating with microglia state (**Fig. 8A, C-E**). It has been previously reported that microglia adopt an amoeboid morphology in PS19 mice, characterized by the loss of microglia processes, and that is associated with a more reactive and phagocytic state[12,86]. We examined microglia morphology in the CA1 in symptomatic mice as we observed the largest decrease in Iba1+ cell counts in this hippocampal region (**Fig. 8B, Supp. 10C-E**). Both the PS19 and PS19;CK2α'$^{(+/-)}$ mice showed a decrease in the average branch length (**Fig. 8C**). However, PS19;CK2α'$^{(+/-)}$ mice demonstrated a significant increase in the number of branches and number of endpoints

compared to the PS19 mice (**Fig. 8D,E**) indicating an improvement in the morphological state of microglia.

Since the morphological state of microglia is strongly related to its reactive state and neuroinflammation, we first assessed the expression of a variety of cytokines and other inflammatory molecules associated with microglia reactivity by using a cytokine array panel with hippocampal extracts from symptomatic PS19 and PS19;CK2α'$^{(+/-)}$ (**Fig. 8F, G**). Importantly, we confirmed that several cytokines were significantly decreased ($p<0.05$) in PS19;CK2α'$^{(+/-)}$ mice relative to PS19 including, MIP-1α, IL17, IL7, IL4, and I309 with several others showing trending decreases ($0.05<p<0.1$) including TREM1 and TNFα (**Fig. 8F, G**). We also investigated whether changes in overall cytokine levels and microglia morphology upon CK2α' depletion related to an altered microglia reactive state. For this we assessed the levels of CD68 in the hippocampus of mice and normalized to the number of Iba1+ cells observed in each animal and time point (**Fig. 9A-E, Supp. Fig. 10I**). We observed increased levels of CD68 in all regions of the hippocampus in the PS19 mice at both prodromal and symptomatic stages (**Fig. 9C-E**)**.** PS19;CK2α'$^{(+/-)}$ mice also presented increased CD68 levels compared to WT but displayed significantly less CD68 in the CA1 and a trending decrease in the CA3 and DG at the prodromal stage compared to PS19 mice (**Fig. 9C-E**). Importantly, symptomatic PS19;CK2α'$^{(+/-)}$ mice displayed significantly less CD68 in all hippocampal regions compared to PS19 mice (**Fig. 9C-E**).

Reactive microglia have also been implicated in synaptic and neuronal loss in tauopathy[80,87-91]. Prior studies have demonstrated that reactivity state of microglia is associated with microglial engulfment of synapses which can be assessed through colocalization of synaptic markers such as PSD95 within microglia[92,93]. To quantify synapse phagocytosis/engulfment we co-stained for PSD95 and Iba1 and examined the CA1 stratum radiatum of symptomatic mice (**Fig. 9F**). PSD95+ puncta were quantified within the Iba1+ cell soma, which is considered to be lysosomes containing degraded material are present[94,95]. PS19 mice exhibited a significant increase in PSD95+ puncta within Iba1+ relative to control mice (**Fig. 9F, G**)**,** demonstrating increased phagocytosis in PS19 microglia. Importantly, PS19;CK2α'$^{(+/-)}$ showed a significant reduction in PSD95+ engulfment (**Fig. 9F, G**) indicating an amelioration in the phagocytic activity of microglia upon deletion of CK2α'.

Discussion

Tauopathies are a heterogeneous group of neurodegenerative disorders for which effective treatments are still not available, in part due to an incomplete understanding of the underlying mechanisms. In this study, we present a novel target, CK2α', a catalytic subunit of CK2, as a potential upstream regulator of tau mediated neurodegeneration, acting at the intersection of immune signaling and synaptic dysfunction.

Here, we report that CK2α' expression is abnormally elevated in the brains of dementia patients and in the hippocampus of PS19 mice, with preferential upregulation observed in hippocampal neurons and microglia. These findings are supported by multiple single-cell RNA-sequencing (snRNA-seq) studies in human AD, which consistently show increased CK2α' expression in excitatory neurons[69-71]. Additionally, the study by Gerrits et al.[68] in the occipital lobe (OL) has

reported preferential CK2α' expression in AD-associated microglia. Other scRNA-seq studies have detected elevated CK2α' expression in various brain cell types, with patterns varying by dataset and brain region[69-71]. Although these datasets lack specific information on the hippocampus, the collective evidence suggests that CK2α' dysregulation in AD/ADRD may be both cell-type- and region-specific.

Increased CK2 levels and/or activity have been previously reported in AD and AD models[19,37,72], and CK2 has been associated with tau pathology[19,20,72,96], microglia state[97,98] and general inflammation[99-105]. However, many of these studies were conducted in cell models[19,20,37,72] and genetic evidence for the specific contributions of the individual CK2 subunits to these processes remained largely unexplored. Our studies in vitro using N2A cells transfected with Tau-P301L showed that silencing CK2α', but not CK2α, decreased pTau accumulation. Furthermore, our studies in vivo reducing the levels of CK2α' in the PS19 model also influenced tau pathology by decreasing the accumulation of pTau and tau burden in the hippocampus and cortex of PS19:CK2α'$^{(+/-)}$ mice. In support to our data, previous studies *in vitro* by Perez et al. showed that overexpression of CK2α' subunit decreased the activity of I2PP2A/SET, a cellular protein that functions as an endogenous inhibitor of protein phosphatase 2A (PP2A), increasing pTau. In contrast overexpression of CK2α increased the activity of I2PPA2a/SET[96]. Although early studies demonstrated that Tau is a physiological substrate of CK2, at least in specific contexts such as neurogenesis[106], the findings by Perez et al.[96] suggest that the effects we observed after manipulating CK2α' on pTau accumulation could be mediated through intermediary molecules that modulate Tau phosphorylation and not directly.

Haploinsufficiency of CK2α' also increased the expression of synaptic genes, synaptic density, and synaptic function in the PS19 mice. Along these lines, haploinsufficiency of CK2α' in a mouse model of HD also showed improved synaptic density and function[18,54], although how exactly CK2α' influences these processes is still unknown. A previous study showed that CK2α' can influence the expression of synaptic genes, especially those related to glutamatergic excitatory signaling[18]. A more recent study showed that pharmacological inhibition of CK2 mitigated AD tau pathology by preventing the NMDA receptor subunit NR2B synaptic mislocalization[72]. NR2B mediates long-term depression (LTD), and LTD specifically induces the phosphorylation of tau. These studies support our findings and strengthen the relationship between CK2α', tau phosphorylation, and the regulation of neuronal function in both AD and other neurodegenerative diseases. However, since CK2α' is found elevated in both neurons and microglia, it is still unknown whether the effects mediated by CK2α' in pTau accumulation and synaptic function are cell or non-cell autonomous, warranting further investigation.

CK2 has been identified as a mediator of microglia reactivity and inflammation in different models[97,98] and it has been well-established as a mediator of inflammation in a variety of contexts including SARS-CoV infection, cancers, bacterial infections, intestinal inflammation and renal failure [99-104]. This is largely mediated via CK2's involvement in regulating several large inflammatory factors such as NF-κB, STAT1, and EGR-1[105]. It is known that chronic activation of NF-kB increases the accumulation of pTau[12]. On the other hand, pathological tau has also been shown to induce inflammation and NF-kB activation by interacting directly with inflammatory receptors such as toll-like receptors 2 (TLR2)[13,14] creating a vicious cycle of worsening

inflammation and tau pathology[12-15]. Our data demonstrated that CK2α' haploinsufficiency significantly reduced the number of Iba1+ cells in the hippocampus, reduced the levels of the microglia reactive marker CD68, ameliorated microglia morphological changes associated with pathology, reduced the levels of pro-inflammatory cytokines in PS19 mice and reduced microglia phagocytic activity. Previous studies in human microglia derived from hiPSCs treated with CK2 inhibitors reduced cytokines production[98]. Therefore, all together, these data support a specific key role of CK2α' in mediating neuroinflammation via activation of microglia.

Loss of synaptic density and neuronal dysfunction has been previously connected to increased phagocytic microglia[64,89,107,108]. The activation of the Complement Component pathway in microglia is associated with enhanced phagocytic activity. While such activation is beneficial to clear Tau aggregates and get rid of dysfunctional synapses, chronic activation results in excessive pruning and an aberrant loss of synapses[80,89]. Our results demonstrated a decrease in microglia phagocytosis of the PSD95 synaptic marker in PS19:CK2α'$^{(+/-)}$ mice suggesting that CK2α' is influencing the phagocytosis of synapses by microglia, but the mechanisms behind this are unclear. Complement component q1 (C1q) is often seen at synapses that accumulate pTau, and the levels of C1q are associated with enhanced phagocytic microglia engulfment of synapses leading to the decline of synapse density, synaptic function and cognitive decline associated with AD[89]. In line with these previous findings, our RNA-seq data revealed the upregulation of genes related to synaptic pruning in PS19 mice, especially those associated with C1q. Importantly, antibodies targeting C1q have rescued synapse loss in tauopathy models[89]. While manipulation of CK2α' did not impact the expression of C1q, it is possible that CK2α' is impacting the complement pathway via phosphorylation of critical components, such as Complement component (C9) and complement component (C1r), which are known targets of CK2 [109,110]. Further studies focusing on the impact of CK2α' on the classical cascade mediated synapse engulfment will be important to elucidate the mechanisms involved in improved synaptic density, function, and cognition.

An intriguing finding from our study is the apparent discrepancy between the upregulation of genes associated with immune and innate responses and the reduction of neuroinflammatory phenotypes in microglia in PS19:CK2α'$^{(+/-)}$ mice. Typically, the transcriptional activation of innate immune pathways is linked to pathology and neuroinflammation. In PS19 mice, such activation, along with increased expression of genes related to microglial dysfunction and reactivity, has been extensively reported[80,81]. Surprisingly, while CK2α' haploinsufficiency further amplified this transcriptional immune response in PS19 mice, we observed a concomitant reduction in neuroinflammatory markers, accompanied by improvements in neuronal function and behavior. This apparent paradox may reflect a primed but non-pathological immune state, the engagement of anti-inflammatory regulatory mechanisms, or a temporal or cell-type-specific decoupling between transcriptional signatures and functional outcomes. Similar findings have been reported in studies involving partial agonists of the tropomyosin receptor kinase B (TrkB) and C (TrkC), where synaptic deficits were rescued in the APP model of AD despite enhanced expression of microglial neuroinflammatory markers and immune responses typically associated with late-stage pathology[111]. Additionally another study reported that INPP5D haploinsufficiency in the PS19 mouse resulted in decreased tau pathology and ameliorated motor deficits[112], yet increased inflammatory signatures seen via RNA-Seq. Collectively, these observations

underscore the nuanced role of immune signaling in the CNS and caution against interpreting transcriptional evidence of inflammation as a direct indicator of detrimental neuroimmune activation.

In conclusion, our findings identify CK2α' as a central and previously underappreciated regulator of tauopathy pathogenesis, acting at the crossroads of immune signaling, synaptic function, and tau phosphorylation. By demonstrating that CK2α' haploinsufficiency alleviates tau pathology, reduces neuroinflammation, and improves synaptic integrity and function in PS19 mice, we provide compelling genetic evidence that CK2α' contributes to multiple pathological hallmarks of tau-driven neurodegeneration. Importantly, these effects appear to occur through complex, context-dependent mechanisms that may differ across cell types and disease stages. The observation that CK2α' influences both neuronal and microglial compartments underscore the need to dissect its cell-autonomous versus non-cell-autonomous roles. Given the growing interest in CK2 as a therapeutic target and the limitations of current inhibitors that lack subunit specificity, the development of CK2α'-selective modulators[113] may represent a promising avenue for disease-modifying therapies in tauopathies and related neurodegenerative conditions. Future studies elucidating the molecular and cellular pathways downstream of CK2α' will be critical for translating these findings into clinical applications.

Figure Legends

Figure 1. CK2α' is increased in tissues of patients with AD/ADRD. **(A, B)** Representative diagram of CK2 holoenzyme, including regulatory and catalytic subunits and differential distribution of expression of catalytic subunits of CK2α and CK2α' in the human body. A and B were created in BioRender (White, A. (2025) eqznm6m https://BioRender.com/). **(C)** Averaged expression of *CSNK2A2* in non-cognitively impaired (NCI) and dementia samples from the Allen Brain Institute: Aging, Dementia and TBI study; parietal cortex (PCx), Temporal cortex (TCx), and Hippocampus (HIP) are shown (patients with TBI were excluded from the analyses). **(E-H)** Quantification of the expression of *CSNK2A2* and *CSNK2A1* in PCx (**E, F**), TCx (**G**), and HIP (**H**) from NCI and dementia from the Allen Brain Institute: Aging, Dementia and TBI study (n=20-27/group). Significance determined by unpaired t-test, *p<0.05. **(I)** Representative immunoblot for CK2α' in protein lysates from frontal cortex of age and sex matched healthy controls (C) and patients with FTD. Arrow indicates CK2α' specific band, asterisk indicates unspecific band. **(J)** CK2α' protein levels were normalized to GAPDH and shown relative to age/sex matched control, quantified using ImageJ software (n=7/group). Data are shown as mean ± SEM. Statistical analyses were conducted using unpaired t-test with welch's correction. * p<0.05. (**K**) Relationship between CK2α' levels from (I) and the presence of Tau pathology reported by the NIH biobank for those samples. Horizontal line represents the group CK2α' intensity average normalized by GAPDH.

Figure 2. *Csnk2a2* expression is increased in both neurons and microglia in the hippocampus of PS19 mice. (A) *Csnk2a2 in situ* hybridization images from symptomatic WT and PS19 hippocampus. Left panels show 10x images of hippocampal cell layers with *Csnk2a2* RNA probe and DAPI, scale bar=50 µm. White boxes indicate zoomed inlets shown on the right panels at 20x, scale bar=10 µm. **(B)** (B) Csnk2a2 in situ hybridization and NeuN immuno-fluorescence images from symptomatic WT and PS19 CA1. Scale bar= 20 µm. (**C-E**) Quantification of *Csnk2a2* puncta in the CA1 (**C**), CA3 (**D**) and DG (**E**) region quantified within the cell layer identified by DAPI, (n=3-4 mice/genotype). **(F)** Representative images *Csnk2a2* RNA probe and Iba1 immunofluorescence in symptomatic WT and PS19 hippocampus. **(G)** Top: representative image of single Iba1+ cell in the Stratum Radiatum (CA1) with *Csnk2a2* RNA Scope. Scale bar is 20 µm. Bottom: 3D rendering of cells Iba1+ cells containing *Csnk2a2* puncta showing puncta reside within the cell. **(H)** Quantification of the number of *Csnk2a2*+ puncta/Iba1+ soma (n=3-4 mice/group, 8-9 cells/mouse, every data point is a cell). All Data shown are mean ± SEM. Statistical analyses were conducted using unpaired t-test * $p<0.05$, *** $p<0.001$, **** $p<0.0001$.

Figure 3. Silencing CK2α' reduces pTau levels in N2a cells expressing Tau-P301L. (A) Schematic of experimental design for N2a cell transfection and immunostaining. **(B)** Representative images of AT8 immunostaining and EGFP fluorescence in N2a cells transfected with either EGFP or Tau-P301L-EGFP and treated with ScrRNA, siCK2α, or siCK2α'. Scale bar= 100 µm. **(C-E)** RT-qPCR analysis of mRNA expression levels of CK2α' **(C)**, CK2α **(D)**, and CK2β **(E)** in transfected N2a cells. Expression levels were normalized to GAPDH and presented relative to ScrRNA EGFP condition (n=3/condition). **(F)** RT-qPCR analysis of mRNA expression levels of huTau expression in N2a cells transfected with EGFP or Tau-P301L-EGFP transfected N2a cells. Expression levels were normalized to GAPDH and presented relative to EGFP condition (n=6/condition). **(G)** Quantification of AT8+ cells normalized to the number of EGFP+ cells, presented relative to ScrRNA Tau-P301L condition. (n=4/condition). All data shown as mean ± SEM. Statistical analyses were conducted using one-way ANOVA with tukey's multiple and displayed with compact letter display. **(H)** Diagram summarizing results of experiment in B. **A** and **H** were created in BioRender (White, A. (2025) https://BioRender.com/eqznm6m).

Figure 4. CK2α' haploinsufficiency reduced tau pathology in PS19 mice. (A) Representative whole-slice sections immunostained for pTau using the AT8 antibody (Ser202/Thr205) in prodromal and symptomatic mice, scale bar= 1000 µm. **(B)** Higher magnification images of hippocampus (CA1, CA3, and DG) from sections shown in (A). Scale bar=500 µm. **(C-E)** Quantification of AT8+ immunoreactivity (% area) in the CA1, CA3 and DG regions in prodromal and symptomatic cohorts (n=6-9 mice/genotype). Data represented as mean ± SEM. Statistical analyses were conducted using two-way ANOVA with tukey's posthoc analysis and displayed with compact letter display. **(E)** Representative pTau pathology types. **(F)** Proportion of each pTau pathology type in prodromal and symptomatic cohorts (n=7-10 mice/genotype). Fisher's exact t-test 7m $p=0.11$ & 12m $p=0.0587$.

Figure 5. CK2α' haploinsufficiency partially rescued hippocampal synapse loss and improved LTP in PS19 mice. (A) Representative NeuN staining in the CA1 of symptomatic mice. Scale bar=200 µm. **(B)** Quantification of NeuN+ cells (cells/mm^2) in the CA1 of prodromal and symptomatic cohorts (n= 3-6 mice/genotype; 2-3 slices/mouse; 1 data point= 1 slice, shape of data point indicates same animal slices). Data was shown as mean ± SEM. Statistical analyses were conducted using one way-ANOVA with Tukey's post-hoc analysis and displayed by compact letter display. Comparisons shown relative to cohort age group. **(C)** Vglut1 and PSD95 immunostaining in the CA1 of symptomatic mice. White arrow heads indicate colocalization of Vglut1 and PSD95. Scale bar= 2.5 µm. **(D-F)** Quantification of PSD95 puncta (**D**), Vglut1 puncta (**E**) and Vglut1/PSD95 colocalized puncta (**F**) relative to WT. (n=3 mice/genotype (3 slices/mouse, 3 images/slice, 1 data point=slice average). **(G-I)** Synaptic analyses from (D-F) represented as a % decrease from WT. Data are shown as mean ± SEM. Statistical analyses were conducted using repeated measures ANOVA with Geisser-greenhouse correction and Tukey's post-hoc analysis *p<0.05, **p<0.01, ***p<0.001, ****p<0.0001. **(J)** Scheme showing the general experimental set-up: R, recording electrode; S stimulating electrode. **(K)** Representative traces before (1) and after (2) the TBS application. **(L)** Course temporal of Theta-burst stimulation (TBS) application inducing LTP in pyramidal neurons of CA1 region from hippocampus (WT, Black n=6; CK2α'$^{(+/-)}$, Grey n=7; PS19, Red, n=7; PS19;CK2α'$^{(+/-)}$, Pink n=6). **(M)** Summary of short-term potentiation (STP) results; significance reported relative to WT. **(N)** Input-output curves. Averaged fEPSP amplitude, (WT, n=3; CK2α'$^{(+/-)}$,n=3; PS19, n=3; PS19;CK2α'$^{(+/-)}$,n=3). (*p < 0.05,**p < 0.01). All data are shown as mean ± SEM. Statistical analyses were conducted using two-sided Student's *t* test or One-way ANOVA with Holm-Sidak multiple comparisons. **(O)** Summary of long-term potentiation (LTP) results; significance reported relative to WT.

Figure 6. Depletion of CK2α' improved spatial memory of PS19 mice on the Barnes maze. (A) Schematic of the Barnes Maze divided into 4 quadrants (Target, Opposite, +1 and -1) and experimental set up. **(B-C)** Primary latency (s), or time to first explore escape hole at prodromal time point. Statistical analyses were conducted using two-way ANOVA with Bonferroni's multiple comparison's. Prodromal; genotype p=0.0573, training day p<0.0001 and interaction p=0.9690. Symptomatic: genotype p<0.0001, training day p<0.0001 and interaction p=0.7018. Differences for each training day were conducted using Bonferroni's multiple comparisons and * show significance relative to WT. **(D)** Time spent in goal quadrant of Barnes maze during probe trial at prodromal and symptomatic time points. n=10-12 mice/genotype, 2 outliers were removed from PS19 group using ROUT (Q=1%). **(E)** Representative search strategy traces based on their navigation patterns on the maze. **(F,H)** Spatial strategies used to locate the escape hole across training days for each genotype at prodromal and symptomatic stages, respectively. **G,I)** Spatial strategies used to locate the previously learned escape target hole during probe trial. Data are shown as mean ± SEM. Statistical analyses were conducted using Two-way ANOVA with Bonferroni's multiple comparisons (B-C) or Two-Way ANOVA with Tukey's post-hoc analysis (D).

Significance displayed with either *p<0.05, **p<0.01, ***p<0.001, ****p<0.0001 or compact letter display.

Figure 7. CK2α' haploinsufficiency has transcriptional impacts on synapses and immune related gene pathways in PS19 mice. (A) Volcano plot of DGEs in PS19 vs WT comparison (n=3-4 mice/genotype). **(B)** Gene-ontology top biological pathways for DGEs in PS19 vs WT. **(C)** Gene network for top 5 synaptic pathways impacted in PS19 vs WT. Red dots indicate genes upregulated in PS19 mice. Blue dots indicate genes down-regulated in PS19 mice. **(D)** Heat map displaying average FC across three comparisons PS19 vs WT, PS19 vs PS19; CK2α'$^{(+/-)}$ and PS19; CK2α'$^{(+/-)}$ vs WT for all significant DGEs identified via PS19 vs PS19; CK2α'$^{(+/-)}$ comparison. Red boxes indicate genes with apoptotic/phagocytotic and or immune-related functions. *q>0.05. **(E)** WGCNA identified modules, dotted line indicates significance as determined by the Kruskal wallis test between WT, CK2α'$^{(+/-)}$, PS19, and PS19:CK2α'$^{(+/-)}$ mice (n=3-5 mice/genotype). **(F)** Heatmap of modules detected from WGCNA indicating differences across genotypes. * indicates p<0.05 determined by Kruskal-wallis test. **(G, H)** Gene ontology for top biological pathways for *MEtan* module (**G**) and *MEturquoise* module (**H**). **(I)** Average representation of pathway activity scores determined via GSVA analysis. Panels **G** and **H** were created in BioRender (White, A. (2025) https://BioRender.com/eqznm6m).

Figure 8. CK2α' haploinsufficiency impacts Iba1+ microglia morphology and cytokine production in PS19 mice. (A) Iba1+ microglia immunostaining and microglia skeleton representation from the CA1 of symptomatic animals used for microglia morphology analysis. **(B)** Quantification of the number of Iba1+ positive cells in the CA1 (n=3-6 mice/genotype). **(C)** Quantification of microglia branch length, **(D)** the number of branches per microglia, **(E)** and number of endpoints per microglia (n=27 cells (3 mice/genotype, 3 slices/mouse, 3 cells/slice). **(F)** Representative cytokine arrays from PS19 and PS19;CK2α'$^{(+/-)}$ at 9 moths from hippocampal protein extracts. Cytokines that showed significant differences are circled in red. **(G)** Selected quantifications of cytokines showing significance or trending significance. Quantifications are represented relative to WT (n=4 mice/genotype). Data are shown as mean ± SEM. Statistical analyses were conducted using ANOVA with Geisser-greenhouse correction and Tukey's post-hoc analysis in **B-E,** and unpaired t-test in **G.** #p<0.1, *p<0.05, **p<0.01, ***p<0.001, ****p<0.0001.

Figure 9. CK2α' haploinsufficiency decreases microglia reactivity and synaptic engulfment. (A) CD68 immunostaining with cresyl violet counterstain in the hippocampus of symptomatic mice. Scale bar=150 µm. (**B**) zoomed images from A in the CA1 and DG. **(C-E)** Quantifications of % area CD68+ normalized by Iba1+ cell count in prodromal and symptomatic cohorts in CA1, CA3 and DG (n=3-6 mice/genotype). Comparisons shown relative to cohort age group. **(F)** Iba1 and PSD95 immunostaining from the CA1 of symptomatic animals. Top row displays whole microglia including processes. Scale bar= 5µm. Middle row displays higher magnification view of the soma (white dotted box in top row), scale bar= 2µm. Bottom row displays 3D reconstruction of Iba1 and PSD95 signal generated from Imaris Software, scale

bar= 2μm. **(G)** Quantification of the number of PSD95 puncta/Iba1+ soma (n= 16-18 cell, 3 mice/genotype, 2-3 slices/mouse, 22 cells/slice). Data are show as mean ± SEM. Statistical analyses were conducted using one-way ANOVA with Tukey's post-hoc *p<0.05, **p<0.01, ***p<0.001, ****p<0.0001.

Supplementary Figure legends

Supplementary Figure 1. *CSNK2a2* scRNA-seq expression in human brain tissue. (A) Summary of *CSNK2a2* single cell expression from studies found in The Alzheimer's Cell Atlas (TACA) in occipital lobe (OL), occipitotemporal cortex (OTC), entorhinal cortex (EC), superior frontal gyrus (SFG), and prefrontal cortex (PFC). Absence of expression for a cell type indicates that cell type was not identified as a cluster in the study.

Supplementary Figure 2. **Generation of a CK2α' haploinsufficient tauopathy model. (A)** The PS19 mouse model was crossed with mice haploinsufficient for CK2α' (Illustration from NIAID NIH BIOART Source (bioart.niaid.nih.gov/bioart/283 & bioart.niaid.nih.gov/bioart/281). **(B)** CK2α' immunoblotting in the hippocampus of symptomatic mice. (**C, D**) Quantification of CK2α' levels from B in CK2α'$^{(+/-)}$ mice relative to WT and PS19;CK2α'$^{(+/-)}$ mice relative to PS19 mice in symptomatic hippocampus (n=6 mice/genotype). Arrow indicates specific CK2α' band. Asterisk indicates an unspecific band. **(E, F)** Relative gene expression of CK2α' in CK2α'$^{(+/-)}$ mice relative to WT and PS19;CK2α'$^{(+/-)}$ mice relative to PS19 mice in the symptomatic hippocampus from qPCR (n=3 mice/genotype). **(G)** Survival curves up to 60 weeks for all 4 genotypes (n=64-74 mice/genotype). Data are shown as mean ± SEM. Statistical analyses were conducted using unpaired t-test *p<0.05, **p<0.01, ***p<0.001.

Supplementary Figure 3. PS19;CK2α'(+/-) mice display decreased AT8 staining in the cortex of symptomatic mice. (A) Representative diagram of cortical region imaged for quantification in B and C. **(B)** Representative images of AT8 staining in the cortex of symptomatic mice. **(B)** Quantification of % area AT8+ in the cortex of prodromal and symptomatic mice (n=3-7 mice/genotype). Data are shown as mean ± SEM. Statistical analyses were conducted using Two-way ANOVA with Tukey's post-hoc analysis and displayed with compact letter display. Panel A was created in BioRender (White, A. (2025) https://BioRender.com/eqznm6m).

Supplementary Figure 4. NeuN pathology and variability among symptomatic PS19 mice. (A) NeuN immunostaining in the hippocampus of prodromal and symptomatic mice. Dotted boxes indicate quantified subregions: CA1, CA3, and DG. Scale bar = 250 μm. **(B-D)** Quantifications of NeuN+ cells (cells/mm^2) in the CA3 (**B**), and DG (**C**) in prodromal and symptomatic cohorts (n= 3-6 mice/genotype;2-3 slices/mouse;1 data point=1 slice, shape of data point indicates slices of the same animal). Data was shown as mean ± SEM. Statistical analyses were conducted using one way-ANOVA with Tukey's post-hoc analysis and displayed

by compact letter display. Comparisons shown relative to cohort age group. **(D)** Representative NeuN immunofluorescence in the hippocampus of symptomatic PS19 mice, demonstrating high and low pathology within littermates. Scale bar=250 µm. **(E)** Quantification of NeuN+ cells in the CA1, CA3 and DG of the hippocampus in high and low pathology mice (n=3 mice/genotype). **(F)** Quantification of hippocampal area in high and low pathology mice (n=3 mice/genotype). Data are shown as mean ± SEM. Statistical analyses were conducted using unpaired t-test. **p<0.01, ***p<0.001.

Supplementary Figure 5. Paired pulse ratio of hippocampal slices shows no deficits between genotypes. (A) Paired-pulse ratio (PPR) in acute hippocampal slices of (WT, Black n=5; CK2α'$^{(+/-)}$, Grey, n=5; PS19, Red, n=5; PS19; CK2α'$^{(+/-)}$, Pink n=4). (*p < 0.05,**p < 0.01). Data are shown as mean ± SEM. Statistical analyses were conducted using two-sided Student's t test. n.s. indicates no significance.

Supplementary Figure 6. Symptomatic PS19 demonstrates decreased movement on Barnes Maze, but hyperactive phenotype in open field. (A-B) Distance traveled in prodromal and symptomatic mice during the probe phase of Barnes Maze. **(C-D)** Distance traveled by prodromal and symptomatic mice during 1 hour in an open field arena. Data are shown as mean ± SEM (n=10-12 mice/genotype, outliers removed using ROUT (Q=1%). Statistical analyses were conducted using One-Way ANOVA with Tukey's post-hoc analysis. *p<0.05, **p<0.01, ***p<0.001, ****p<0.0001.

Supplementary Figure 7. RNA-Seq analyses in PS19 cohort show genetic variability associated with high and low pathology. (A) Representative AT8 staining of a low and high pathology prodromal PS19 mice scale bar= 1000 µm. **(B)** Gene ontology top related pathways for Low pathology PS19 vs WT. **(C)** Gene ontology top related pathways for High pathology PS19 vs WT comparison. **(D-E)** Venn diagram of the number of unique and overlapping DGEs for 6 total comparisons of interest.

Supplementary Figure 8. PS19;CK2α'(+/-) mice display increased immune-related gene expression. (A) Eigengene Average expression for tan module. **(A)** Eigengene Average expression for turquoise module. **(C)** Gene ontology for the top-related pathways for the DGEs in PS19 vs WT not present in the PS19;CK2α'$^{(+/-)}$ vs WT comparison. **(D)** Gene ontology for the top-related pathways for the DGEs in PS19;CK2α'$^{(+/-)}$ vs WT not present in the PS19 vs WT comparison. **(E)** Gene network for the top 2 pathways returned in (D).

Supplementary Figure 9. CK2α' haploinsufficency decreased GFAP+ astrocytes in the overlaying cortex but not in the hippocampus of PS19 mice. (A-B) Immunostaining for

GFAP in the CA1, CA3 and DG of the hippocampus in prodromal (A) and symptomatic (B) cohorts. Scale bar=100 µm. **(C-E)** Quantification of GFAP+ cells in CA1, CA3 and DG of hippocampus. (n=3-6 mice/genotype). **(F)** Representative area corresponding to overlying cortex is indicated with a boxed area. **(G)** Representative GFAP immunostaining in the cortex. Scale bar= 50 µm. **(H)** Quantification of GFAP+ cells in the cortex (n=3-6/genotype). All Data are shown as mean ± SEM. Statistical analyses were conducted using two-way ANOVA with tukey's multiple corrections and represented with compact letter display. Panel **F** was created in BioRender (White, A. (2025) https://BioRender.com/eqznm6m).

Supplementary Figure 10. CK2α' haploinsufficency decreased Iba1+ microglia cell number in the hippocampus and overlaying cortex of PS19 mice. (A-B) Immunostaining for Iba1 in the CA1, CA3 and DG of the hippocampus in prodromal (**A**) and symptomatic (**B**) cohorts. Scale bar=100 µm. **(C-E)** Quantification of Iba1+ cell counts in CA1, CA3 and DG of hippocampus (n=3-6 mice/genotype). **(F)** Representative area corresponding to overlying cortex is indicated with a boxed area. **(G)** Representative Iba1 immunostaining in the cortex scale bar=50 µm. **(H)** Quantification of Iba1+ cells in the cortex (n=3-6 mice/genotype). All data are shown as mean ± SEM. Statistical analyses were conducted using two-way ANOVA with tukey's multiple corrections and represented with compact letter display. Panel **F** was created in BioRender (White, A. (2025) https://BioRender.com/eqznm6m).

References

1. Kovacech B, Skrabana R, Novak M. Transition of tau protein from disordered to misordered in Alzheimer's disease. *Neurodegener Dis*. 2010;7(1-3):24-7. doi:10.1159/000283478
2. Lee VM, Goedert M, Trojanowski JQ. Neurodegenerative tauopathies. *Annu Rev Neurosci*. 2001;24:1121-59. doi:10.1146/annurev.neuro.24.1.1121
3. Josephs KA, Hodges JR, Snowden JS, et al. Neuropathological background of phenotypical variability in frontotemporal dementia. *Acta Neuropathol*. Aug 2011;122(2):137-53. doi:10.1007/s00401-011-0839-6
4. Weingarten MD, Lockwood AH, Hwo SY, Kirschner MW. A protein factor essential for microtubule assembly. *Proc Natl Acad Sci U S A*. May 1975;72(5):1858-62. doi:10.1073/pnas.72.5.1858
5. Strang KH, Golde TE, Giasson BI. MAPT mutations, tauopathy, and mechanisms of neurodegeneration. *Lab Invest*. Jul 2019;99(7):912-928. doi:10.1038/s41374-019-0197-x
6. Sexton C, Snyder H, Beher D, et al. Current directions in tau research: Highlights from Tau 2020. *Alzheimers Dement*. May 2022;18(5):988-1007. doi:10.1002/alz.12452
7. Tai HC, Serrano-Pozo A, Hashimoto T, Frosch MP, Spires-Jones TL, Hyman BT. The synaptic accumulation of hyperphosphorylated tau oligomers in Alzheimer disease is associated with dysfunction of the ubiquitin-proteasome system. *Am J Pathol*. Oct 2012;181(4):1426-35. doi:10.1016/j.ajpath.2012.06.033

8. Dani M, Wood M, Mizoguchi R, et al. Microglial activation correlates in vivo with both tau and amyloid in Alzheimer's disease. *Brain*. Sep 01 2018;141(9):2740-2754. doi:10.1093/brain/awy188

9. Lee SH, Bae EJ, Park SJ, Lee SJ. Microglia-driven inflammation induces progressive tauopathies and synucleinopathies. *Exp Mol Med*. May 01 2025;doi:10.1038/s12276-025-01450-z

10. Bejanin A, Schonhaut DR, La Joie R, et al. Tau pathology and neurodegeneration contribute to cognitive impairment in Alzheimer's disease. *Brain*. Dec 01 2017;140(12):3286-3300. doi:10.1093/brain/awx243

11. Langworth-Green C, Patel S, Jaunmuktane Z, et al. Chronic effects of inflammation on tauopathies. *Lancet Neurol*. May 2023;22(5):430-442. doi:10.1016/S1474-4422(23)00038-8

12. Wang C, Fan L, Khawaja RR, et al. Microglial NF-κB drives tau spreading and toxicity in a mouse model of tauopathy. *Nat Commun*. Apr 12 2022;13(1):1969. doi:10.1038/s41467-022-29552-6

13. Kim Y, Ryu SH, Hyun J, Cho YS, Jung YK. TLR2 immunotherapy suppresses neuroinflammation, tau spread, and memory loss in rTg4510 mice. *Brain Behav Immun*. Oct 2024;121:291-302. doi:10.1016/j.bbi.2024.08.002

14. Dutta D, Jana M, Paidi RK, et al. Tau fibrils induce glial inflammation and neuropathology via TLR2 in Alzheimer's disease-related mouse models. *J Clin Invest*. Sep 15 2023;133(18)doi:10.1172/JCI161987

15. Bhaskar K, Konerth M, Kokiko-Cochran ON, Cardona A, Ransohoff RM, Lamb BT. Regulation of tau pathology by the microglial fractalkine receptor. *Neuron*. Oct 06 2010;68(1):19-31. doi:10.1016/j.neuron.2010.08.023

16. Litchfield DW. Protein kinase CK2: structure, regulation and role in cellular decisions of life and death. *Biochem J*. Jan 01 2003;369(Pt 1):1-15. doi:10.1042/BJ20021469

17. Gomez-Pastor R, Burchfiel ET, Neef DW, et al. Abnormal degradation of the neuronal stress-protective transcription factor HSF1 in Huntington's disease. *Nat Commun*. 02 13 2017;8:14405. doi:10.1038/ncomms14405

18. Yu D, Zarate N, White A, et al. CK2 alpha prime and alpha-synuclein pathogenic functional interaction mediates synaptic dysregulation in huntington's disease. *Acta Neuropathol Commun*. Jun 03 2022;10(1):83. doi:10.1186/s40478-022-01379-8

19. Zhang Q, Xia Y, Wang Y, et al. CK2 Phosphorylating I 2 PP2A /SET Mediates Tau Pathology and Cognitive Impairment. *Front Mol Neurosci*. 2018;11:146. doi:10.3389/fnmol.2018.00146

20. Yadikar H, Torres I, Aiello G, et al. Screening of tau protein kinase inhibitors in a tauopathy-relevant cell-based model of tau hyperphosphorylation and oligomerization. *PLoS One*. 2020;15(7):e0224952. doi:10.1371/journal.pone.0224952

21. Baum L, Masliah E, Iimoto DS, Hansen LA, Halliday WC, Saitoh T. Casein kinase II is associated with neurofibrillary tangles but is not an intrinsic component of paired helical filaments. *Brain Res*. Feb 21 1992;573(1):126-32. doi:10.1016/0006-8993(92)90121-o

22. Lim AC, Tiu SY, Li Q, Qi RZ. Direct regulation of microtubule dynamics by protein kinase CK2. *J Biol Chem*. Feb 06 2004;279(6):4433-9. doi:10.1074/jbc.M310563200

23. Chung HJ, Huang YH, Lau LF, Huganir RL. Regulation of the NMDA receptor complex and trafficking by activity-dependent phosphorylation of the NR2B subunit PDZ ligand. *J Neurosci*. Nov 10 2004;24(45):10248-59. doi:10.1523/JNEUROSCI.0546-04.2004

24. Kimura R, Matsuki N. Protein kinase CK2 modulates synaptic plasticity by modification of synaptic NMDA receptors in the hippocampus. *J Physiol*. Jul 01 2008;586(13):3195-206. doi:10.1113/jphysiol.2008.151894

25. Lenzken SC, Stanga S, Lanni C, De Leonardis F, Govoni S, Racchi M. Recruitment of casein kinase 2 is involved in AbetaPP processing following cholinergic stimulation. *J Alzheimers Dis*. 2010;20(4):1133-41. doi:10.3233/JAD-2010-090232

26. Raftery M, Campbell R, Glaros EN, et al. Phosphorylation of apolipoprotein-E at an atypical protein kinase CK2 PSD/E site in vitro. *Biochemistry*. May 17 2005;44(19):7346-53. doi:10.1021/bi0504052

27. Walter J, Schindzielorz A, Hartung B, Haass C. Phosphorylation of the beta-amyloid precursor protein at the cell surface by ectocasein kinases 1 and 2. *J Biol Chem*. Aug 04 2000;275(31):23523-9. doi:10.1074/jbc.M002850200

28. Bian Y, Ye M, Wang C, et al. Global screening of CK2 kinase substrates by an integrated phosphoproteomics workflow. *Sci Rep*. Dec 10 2013;3:3460. doi:10.1038/srep03460

29. Rusin SF, Adamo ME, Kettenbach AN. Identification of Candidate Casein Kinase 2 Substrates in Mitosis by Quantitative Phosphoproteomics. *Front Cell Dev Biol*. 2017;5:97. doi:10.3389/fcell.2017.00097

30. Guerra B, Siemer S, Boldyreff B, Issinger OG. Protein kinase CK2: evidence for a protein kinase CK2beta subunit fraction, devoid of the catalytic CK2alpha subunit, in mouse brain and testicles. *FEBS Lett*. Dec 03 1999;462(3):353-7. doi:10.1016/s0014-5793(99)01553-7

31. Montenarh M, Götz C. Protein Kinase CK2α', More than a Backup of CK2α. *Cells*. Dec 14 2023;12(24)doi:10.3390/cells12242834

32. Ceglia I, Flajolet M, Rebholz H. Predominance of CK2α over CK2α' in the mammalian brain. *Mol Cell Biochem*. Oct 2011;356(1-2):169-75. doi:10.1007/s11010-011-0963-6

33. Lou DY, Dominguez I, Toselli P, Landesman-Bollag E, O'Brien C, Seldin DC. The alpha catalytic subunit of protein kinase CK2 is required for mouse embryonic development. *Mol Cell Biol*. Jan 2008;28(1):131-9. doi:10.1128/MCB.01119-07

34. Xu X, Toselli PA, Russell LD, Seldin DC. Globozoospermia in mice lacking the casein kinase II alpha' catalytic subunit. *Nat Genet*. Sep 1999;23(1):118-21. doi:10.1038/12729

35. Iimoto DS, Masliah E, DeTeresa R, Terry RD, Saitoh T. Aberrant casein kinase II in Alzheimer's disease. *Brain Res*. Jan 22 1990;507(2):273-80. doi:10.1016/0006-8993(90)90282-g

36. Allende JE, Allende CC. Protein kinases. 4. Protein kinase CK2: an enzyme with multiple substrates and a puzzling regulation. *FASEB J*. Mar 1995;9(5):313-23. doi:10.1096/fasebj.9.5.7896000

37. Rosenberger AF, Morrema TH, Gerritsen WH, et al. Increased occurrence of protein kinase CK2 in astrocytes in Alzheimer's disease pathology. *J Neuroinflammation*. Jan 06 2016;13:4. doi:10.1186/s12974-015-0470-x

38. Aksenova MV, Burbaeva GS, Kandror KV, Kapkov DV, Stepanov AS. The decreased level of casein kinase 2 in brain cortex of schizophrenic and Alzheimer's disease patients. *FEBS Lett*. Feb 11 1991;279(1):55-7. doi:10.1016/0014-5793(91)80249-3

39. Saitoh T, Iimoto D. Aberrant protein phosphorylation and cytoarchitecture in Alzheimer's disease. *Prog Clin Biol Res*. 1989;317:769-80.

40. Yoshiyama Y, Higuchi M, Zhang B, et al. Synapse loss and microglial activation precede tangles in a P301S tauopathy mouse model. *Neuron*. Feb 01 2007;53(3):337-51. doi:10.1016/j.neuron.2007.01.010

41. Wauters M, Wattiez R, Ris L. Internalization of the Extracellular Full-Length Tau Inside Neuro2A and Cortical Cells Is Enhanced by Phosphorylation. *Biomolecules*. Aug 19 2016;6(3)doi:10.3390/biom6030036

42. Namsi A, Nury T, Hamdouni H, et al. Induction of Neuronal Differentiation of Murine N2a Cells by Two Polyphenols Present in the Mediterranean Diet Mimicking Neurotrophins Activities: Resveratrol and Apigenin. *Diseases*. Jul 22 2018;6(3)doi:10.3390/diseases6030067

43. Hoover BR, Reed MN, Su J, et al. Tau mislocalization to dendritic spines mediates synaptic dysfunction independently of neurodegeneration. *Neuron*. Dec 22 2010;68(6):1067-81. doi:10.1016/j.neuron.2010.11.030

44. Brown TG, Thayer MN, VanTreeck JG, et al. Striatal spatial heterogeneity, clustering, and white matter association of GFAP. *Front Cell Neurosci*. 2023;17:1094503. doi:10.3389/fncel.2023.1094503
45. Solem MA, G Pelzel R, Rozema NB, et al. Absence of hippocampal pathology persists in the Q175DN mouse model of Huntington's disease despite elevated HTT aggregation. *J Huntingtons Dis*. Feb 2025;14(1):59-84. doi:10.1177/18796397251316762
46. Shi Y, Yamada K, Liddelow SA, et al. ApoE4 markedly exacerbates tau-mediated neurodegeneration in a mouse model of tauopathy. *Nature*. Sep 28 2017;549(7673):523-527. doi:10.1038/nature24016
47. Shi Y, Manis M, Long J, et al. Microglia drive APOE-dependent neurodegeneration in a tauopathy mouse model. *J Exp Med*. Nov 04 2019;216(11):2546-2561. doi:10.1084/jem.20190980
48. Martini-Stoica H, Cole AL, Swartzlander DB, et al. TFEB enhances astroglial uptake of extracellular tau species and reduces tau spreading. *J Exp Med*. Sep 03 2018;215(9):2355-2377. doi:10.1084/jem.20172158
49. Takahashi H, Bhagwagar S, Nies SH, et al. Reduced progranulin increases tau and α-synuclein inclusions and alters mouse tauopathy phenotypes via glucocerebrosidase. *Nat Commun*. Feb 16 2024;15(1):1434. doi:10.1038/s41467-024-45692-3
50. Bankhead P, Loughrey MB, Fernández JA, et al. QuPath: Open source software for digital pathology image analysis. *Sci Rep*. Dec 04 2017;7(1):16878. doi:10.1038/s41598-017-17204-5
51. Schindelin J, Arganda-Carreras I, Frise E, et al. Fiji: an open-source platform for biological-image analysis. *Nat Methods*. Jun 28 2012;9(7):676-82. doi:10.1038/nmeth.2019
52. Ruifrok AC, Johnston DA. Quantification of histochemical staining by color deconvolution. *Anal Quant Cytol Histol*. Aug 2001;23(4):291-9.
53. Zarate N, Intihar TA, Yu D, et al. Heat Shock Factor 1 Directly Regulates Postsynaptic Scaffolding PSD-95 in Aging and Huntington's Disease and Influences Striatal Synaptic Density. *Int J Mol Sci*. Dec 04 2021;22(23)doi:10.3390/ijms222313113
54. Zarate N, Gundry K, Yu D, et al. Neurochemical correlates of synapse density in a Huntington's disease mouse model. *J Neurochem*. Jan 2023;164(2):226-241. doi:10.1111/jnc.15714
55. McKinstry SU, Karadeniz YB, Worthington AK, et al. Huntingtin is required for normal excitatory synapse development in cortical and striatal circuits. *J Neurosci*. Jul 09 2014;34(28):9455-72. doi:10.1523/JNEUROSCI.4699-13.2014
56. Pitts MW. Barnes Maze Procedure for Spatial Learning and Memory in Mice. *Bio Protoc*. Mar 05 2018;8(5)doi:10.21769/bioprotoc.2744
57. Illouz T, Madar R, Clague C, Griffioen KJ, Louzoun Y, Okun E. Unbiased classification of spatial strategies in the Barnes maze. *Bioinformatics*. Nov 01 2016;32(21):3314-3320. doi:10.1093/bioinformatics/btw376
58. Barnes CA. Memory deficits associated with senescence: a neurophysiological and behavioral study in the rat. *J Comp Physiol Psychol*. Feb 1979;93(1):74-104. doi:10.1037/h0077579
59. Love MI, Huber W, Anders S. Moderated estimation of fold change and dispersion for RNA-seq data with DESeq2. *Genome Biol*. 2014;15(12):550. doi:10.1186/s13059-014-0550-8
60. Raudvere U, Kolberg L, Kuzmin I, et al. g:Profiler: a web server for functional enrichment analysis and conversions of gene lists (2019 update). *Nucleic Acids Res*. Jul 02 2019;47(W1):W191-W198. doi:10.1093/nar/gkz369
61. Young K, Morrison H. Quantifying Microglia Morphology from Photomicrographs of Immunohistochemistry Prepared Tissue Using ImageJ. *J Vis Exp*. Jun 05 2018;(136)doi:10.3791/57648

62. Arganda-Carreras I, Fernández-González R, Muñoz-Barrutia A, Ortiz-De-Solorzano C. 3D reconstruction of histological sections: Application to mammary gland tissue. *Microsc Res Tech*. Oct 2010;73(11):1019-29. doi:10.1002/jemt.20829
63. Miller JA, Guillozet-Bongaarts A, Gibbons LE, et al. Neuropathological and transcriptomic characteristics of the aged brain. *Elife*. Nov 09 2017;6doi:10.7554/eLife.31126
64. Walker CK, Greathouse KM, Boros BD, et al. Dendritic Spine Remodeling and Synaptic Tau Levels in PS19 Tauopathy Mice. *Neuroscience*. Feb 10 2021;455:195-211. doi:10.1016/j.neuroscience.2020.12.006
65. Takeuchi H, Iba M, Inoue H, et al. P301S mutant human tau transgenic mice manifest early symptoms of human tauopathies with dementia and altered sensorimotor gating. *PLoS One*. 2011;6(6):e21050. doi:10.1371/journal.pone.0021050
66. Zhang B, Carroll J, Trojanowski JQ, et al. The microtubule-stabilizing agent, epothilone D, reduces axonal dysfunction, neurotoxicity, cognitive deficits, and Alzheimer-like pathology in an interventional study with aged tau transgenic mice. *J Neurosci*. Mar 14 2012;32(11):3601-11. doi:10.1523/JNEUROSCI.4922-11.2012
67. Zhou Y, Xu J, Hou Y, et al. The Alzheimer's Cell Atlas (TACA): A single-cell molecular map for translational therapeutics accelerator in Alzheimer's disease. *Alzheimers Dement (N Y)*. 2022;8(1):e12350. doi:10.1002/trc2.12350
68. Gerrits E, Brouwer N, Kooistra SM, et al. Distinct amyloid-β and tau-associated microglia profiles in Alzheimer's disease. *Acta Neuropathol*. May 2021;141(5):681-696. doi:10.1007/s00401-021-02263-w
69. Otero-Garcia M, Mahajani SU, Wakhloo D, et al. Molecular signatures underlying neurofibrillary tangle susceptibility in Alzheimer's disease. *Neuron*. Sep 21 2022;110(18):2929-2948.e8. doi:10.1016/j.neuron.2022.06.021
70. Leng K, Li E, Eser R, et al. Molecular characterization of selectively vulnerable neurons in Alzheimer's disease. *Nat Neurosci*. Feb 2021;24(2):276-287. doi:10.1038/s41593-020-00764-7
71. Lau SF, Cao H, Fu AKY, Ip NY. Single-nucleus transcriptome analysis reveals dysregulation of angiogenic endothelial cells and neuroprotective glia in Alzheimer's disease. *Proc Natl Acad Sci U S A*. Oct 13 2020;117(41):25800-25809. doi:10.1073/pnas.2008762117
72. Marshall CA, McBride JD, Changolkar L, Riddle DM, Trojanowski JQ, Lee VM. Inhibition of CK2 mitigates Alzheimer's tau pathology by preventing NR2B synaptic mislocalization. *Acta Neuropathol Commun*. 03 04 2022;10(1):30. doi:10.1186/s40478-022-01331-w
73. Sahara N, Yanai R. Limitations of human tau-expressing mouse models and novel approaches of mouse modeling for tauopathy. *Front Neurosci*. 2023;17:1149761. doi:10.3389/fnins.2023.1149761
74. Choi YB, Dunn-Meynell AA, Marchese M, et al. Erythropoietin-derived peptide treatment reduced neurological deficit and neuropathological changes in a mouse model of tauopathy. *Alzheimers Res Ther*. Jan 27 2021;13(1):32. doi:10.1186/s13195-020-00766-4
75. DeVos SL, Miller RL, Schoch KM, et al. Tau reduction prevents neuronal loss and reverses pathological tau deposition and seeding in mice with tauopathy. *Sci Transl Med*. Jan 25 2017;9(374)doi:10.1126/scitranslmed.aag0481
76. Wagner J, Krauss S, Shi S, et al. Reducing tau aggregates with anle138b delays disease progression in a mouse model of tauopathies. *Acta Neuropathol*. Nov 2015;130(5):619-31. doi:10.1007/s00401-015-1483-3
77. Crescenzi R, DeBrosse C, Nanga RP, et al. In vivo measurement of glutamate loss is associated with synapse loss in a mouse model of tauopathy. *Neuroimage*. Nov 01 2014;101:185-92. doi:10.1016/j.neuroimage.2014.06.067
78. Zheng N, Li K, Cao J, et al. Electrophysiology-based screening identifies neuronal HtrA serine peptidase 2 (HTRA2) as a synaptic plasticity regulator participating in tauopathy. *Transl Psychiatry*. Jan 10 2025;15(1):5. doi:10.1038/s41398-025-03227-4

79. El Fatimy R, Li S, Chen Z, et al. MicroRNA-132 provides neuroprotection for tauopathies via multiple signaling pathways. *Acta Neuropathol*. Oct 2018;136(4):537-555. doi:10.1007/s00401-018-1880-5

80. Litvinchuk A, Wan YW, Swartzlander DB, et al. Complement C3aR Inactivation Attenuates Tau Pathology and Reverses an Immune Network Deregulated in Tauopathy Models and Alzheimer's Disease. *Neuron*. Dec 19 2018;100(6):1337-1353.e5. doi:10.1016/j.neuron.2018.10.031

81. Kim J, Selvaraji S, Kang SW, et al. Cerebral transcriptome analysis reveals age-dependent progression of neuroinflammation in P301S mutant tau transgenic male mice. *Brain Behav Immun*. Aug 2019;80:344-357. doi:10.1016/j.bbi.2019.04.011

82. Chen X, Firulyova M, Manis M, et al. Microglia-mediated T cell infiltration drives neurodegeneration in tauopathy. *Nature*. Mar 2023;615(7953):668-677. doi:10.1038/s41586-023-05788-0

83. Odfalk KF, Bieniek KF, Hopp SC. Microglia: Friend and foe in tauopathy. *Prog Neurobiol*. Sep 2022;216:102306. doi:10.1016/j.pneurobio.2022.102306

84. Gao C, Jiang J, Tan Y, Chen S. Microglia in neurodegenerative diseases: mechanism and potential therapeutic targets. *Signal Transduct Target Ther*. Sep 22 2023;8(1):359. doi:10.1038/s41392-023-01588-0

85. Fixemer S, Ameli C, Hammer G, et al. Microglia phenotypes are associated with subregional patterns of concomitant tau, amyloid-β and α-synuclein pathologies in the hippocampus of patients with Alzheimer's disease and dementia with Lewy bodies. *Acta Neuropathol Commun*. Mar 16 2022;10(1):36. doi:10.1186/s40478-022-01342-7

86. Leyh J, Paeschke S, Mages B, et al. Classification of Microglial Morphological Phenotypes Using Machine Learning. *Front Cell Neurosci*. 2021;15:701673. doi:10.3389/fncel.2021.701673

87. Hassan-Abdi R, Brenet A, Bennis M, Yanicostas C, Soussi-Yanicostas N. Neurons Expressing Pathological Tau Protein Trigger Dramatic Changes in Microglial Morphology and Dynamics. *Front Neurosci*. 2019;13:1199. doi:10.3389/fnins.2019.01199

88. Hong S, Beja-Glasser VF, Nfonoyim BM, et al. Complement and microglia mediate early synapse loss in Alzheimer mouse models. *Science*. May 06 2016;352(6286):712-716. doi:10.1126/science.aad8373

89. Dejanovic B, Huntley MA, De Mazière A, et al. Changes in the Synaptic Proteome in Tauopathy and Rescue of Tau-Induced Synapse Loss by C1q Antibodies. *Neuron*. Dec 19 2018;100(6):1322-1336.e7. doi:10.1016/j.neuron.2018.10.014

90. Lui H, Zhang J, Makinson SR, et al. Progranulin Deficiency Promotes Circuit-Specific Synaptic Pruning by Microglia via Complement Activation. *Cell*. May 05 2016;165(4):921-35. doi:10.1016/j.cell.2016.04.001

91. Pampuscenko K, Morkuniene R, Krasauskas L, Smirnovas V, Brown GC, Borutaite V. Extracellular tau stimulates phagocytosis of living neurons by activated microglia via Toll-like 4 receptor-NLRP3 inflammasome-caspase-1 signalling axis. *Sci Rep*. Jul 04 2023;13(1):10813. doi:10.1038/s41598-023-37887-3

92. Parhizkar S, Bao X, Chen W, et al. Lemborexant ameliorates tau-mediated sleep loss and neurodegeneration in males in a mouse model of tauopathy. *Nat Neurosci*. May 27 2025;doi:10.1038/s41593-025-01966-7

93. Roy ER, Chiu G, Li S, et al. Concerted type I interferon signaling in microglia and neural cells promotes memory impairment associated with amyloid β plaques. *Immunity*. May 10 2022;55(5):879-894.e6. doi:10.1016/j.immuni.2022.03.018

94. El Hajj H, Savage JC, Bisht K, et al. Ultrastructural evidence of microglial heterogeneity in Alzheimer's disease amyloid pathology. *J Neuroinflammation*. Apr 16 2019;16(1):87. doi:10.1186/s12974-019-1473-9

95. Möller K, Brambach M, Villani A, Gallo E, Gilmour D, Peri F. A role for the centrosome in regulating the rate of neuronal efferocytosis by microglia in vivo. *Elife*. Nov 18 2022;11doi:10.7554/eLife.82094

96. Pérez M, Avila J. The expression of casein kinase 2alpha' and phosphatase 2A activity. *Biochim Biophys Acta*. Mar 08 1999;1449(2):150-6. doi:10.1016/s0167-4889(99)00008-7

97. Liu J, Tian J, Xie R, Chen L. CK2 inhibitor DMAT ameliorates spinal cord injury by increasing autophagy and inducing anti-inflammatory microglial polarization. *Neurosci Lett*. May 14 2023;805:137222. doi:10.1016/j.neulet.2023.137222

98. Mishra S, Kinoshita C, Axtman AD, Young JE. Evaluation of a Selective Chemical Probe Validates That CK2 Mediates Neuroinflammation in a Human Induced Pluripotent Stem Cell-Derived Microglial Model. *Front Mol Neurosci*. 2022;15:824956. doi:10.3389/fnmol.2022.824956

99. Chen IY, Chang SC, Wu HY, et al. Upregulation of the chemokine (C-C motif) ligand 2 via a severe acute respiratory syndrome coronavirus spike-ACE2 signaling pathway. *J Virol*. Aug 2010;84(15):7703-12. doi:10.1128/JVI.02560-09

100. Larson SR, Bortell N, Illies A, Crisler WJ, Matsuda JL, Lenz LL. Myeloid Cell CK2 Regulates Inflammation and Resistance to Bacterial Infection. *Front Immunol*. 2020;11:590266. doi:10.3389/fimmu.2020.590266

101. Drygin D, Ho CB, Omori M, et al. Protein kinase CK2 modulates IL-6 expression in inflammatory breast cancer. *Biochem Biophys Res Commun*. Nov 11 2011;415(1):163-7. doi:10.1016/j.bbrc.2011.10.046

102. Parhar K, Morse J, Salh B. The role of protein kinase CK2 in intestinal epithelial cell inflammatory signaling. *Int J Colorectal Dis*. Jun 2007;22(6):601-9. doi:10.1007/s00384-006-0193-7

103. Yamada M, Katsuma S, Adachi T, et al. Inhibition of protein kinase CK2 prevents the progression of glomerulonephritis. *Proc Natl Acad Sci U S A*. May 24 2005;102(21):7736-41. doi:10.1073/pnas.0409818102

104. Huang J, Li J, Chen Z, et al. Sphingosine kinase 1 mediates diabetic renal fibrosis via NF-κB signaling pathway: involvement of CK2α. *Oncotarget*. Oct 24 2017;8(51):88988-89004. doi:10.18632/oncotarget.21640

105. Singh NN, Ramji DP. Protein kinase CK2, an important regulator of the inflammatory response? *J Mol Med (Berl)*. Aug 2008;86(8):887-97. doi:10.1007/s00109-008-0352-0

106. Avila J, Ulloa L, González J, Moreno F, Díaz-Nido J. Phosphorylation of microtubule-associated proteins by protein kinase CK2 in neuritogenesis. *Cell Mol Biol Res*. 1994;40(5-6):573-9.

107. Coomans EM, Schoonhoven DN, Tuncel H, et al. In vivo tau pathology is associated with synaptic loss and altered synaptic function. *Alzheimers Res Ther*. Feb 05 2021;13(1):35. doi:10.1186/s13195-021-00772-0

108. Vogels T, Murgoci AN, Hromádka T. Intersection of pathological tau and microglia at the synapse. *Acta Neuropathol Commun*. Jul 05 2019;7(1):109. doi:10.1186/s40478-019-0754-y

109. Bohana-Kashtan O, Pinna LA, Fishelson Z. Extracellular phosphorylation of C9 by protein kinase CK2 regulates complement-mediated lysis. *Eur J Immunol*. Jun 2005;35(6):1939-48. doi:10.1002/eji.200425716

110. Pelloux S, Thielens NM, Hudry-Clergeon G, Pétillot Y, Filhol O, Arlaud GJ. Identification of a cryptic protein kinase CK2 phosphorylation site in human complement protease Clr, and its use to probe intramolecular interaction. *FEBS Lett*. May 13 1996;386(1):15-20. doi:10.1016/0014-5793(96)00403-6

111. Latif-Hernandez A, Yang T, Butler RR, et al. A TrkB and TrkC partial agonist restores deficits in synaptic function and promotes activity-dependent synaptic and microglial transcriptomic changes in a late-stage Alzheimer's mouse model. *Alzheimers Dement*. Jul 2024;20(7):4434-4460. doi:10.1002/alz.13857

112. Soni DM, Lin PB, Lee-Gosselin A, et al. Inpp5d haplodeficiency alleviates tau pathology in the PS19 mouse model of Tauopathy. *Alzheimers Dement*. Jul 2024;20(7):4985-4998. doi:10.1002/alz.14078

113. Mudaliar D, Mansky RH, White A, et al. Discovery of a CK2α'-Biased ATP-Competitive Inhibitor from a High-Throughput Screen of an Allosteric-Inhibitor-Like Compound Library. *ACS Chem Neurosci*. Jun 22 2024;doi:10.1021/acschemneuro.4c00062

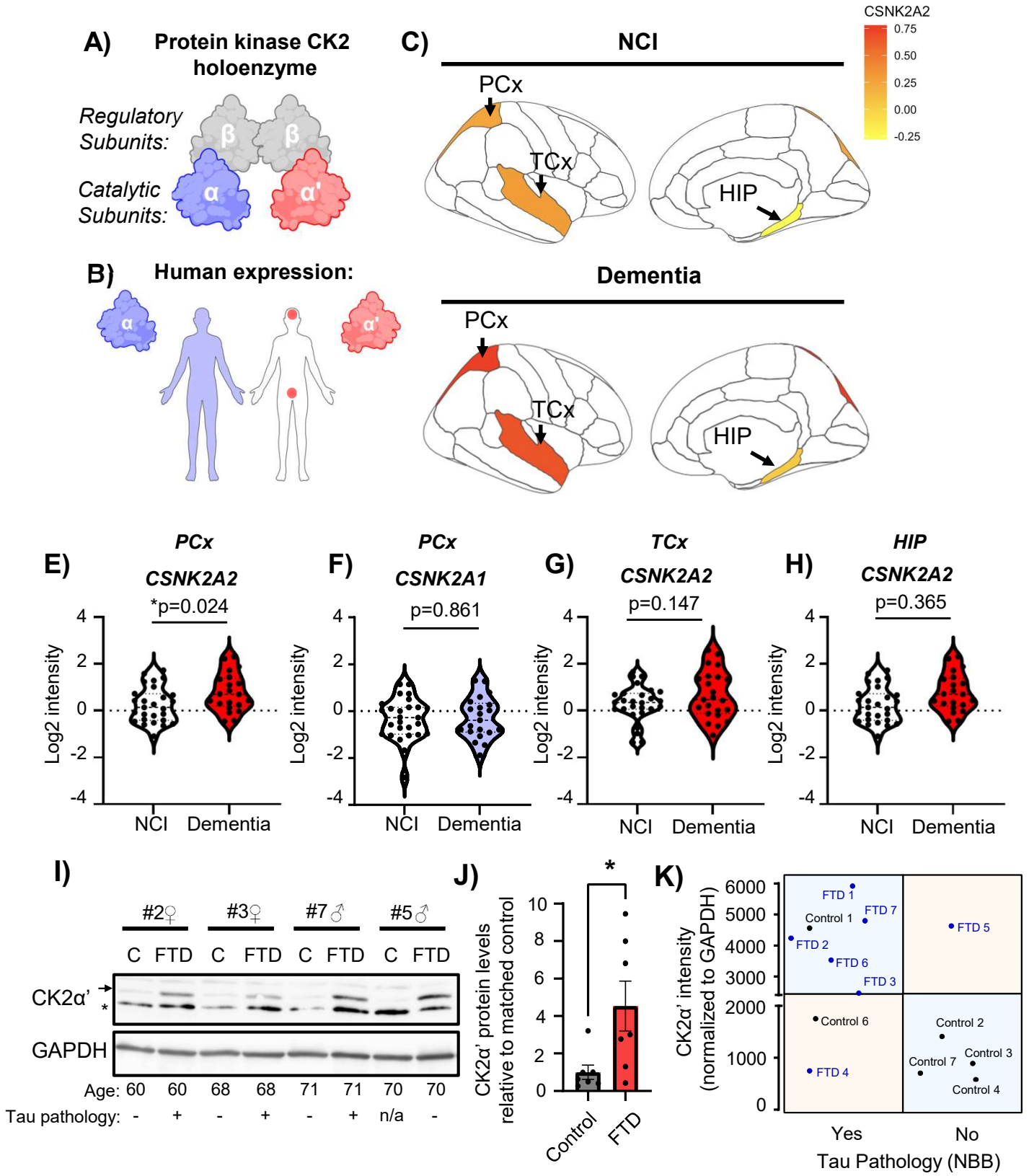
A)
Protein kinase CK2 holoenzyme
Regulatory Subunits:
Catalytic Subunits:
β
β
α
α'
B)
Human expression:
α
α'
C)
NCI
Dementia
PCx
TCx
HIP
CSNK2A2
0.75
0.50
0.25
0.00
-0.25
E)
PCx
CSNK2A2
*p=0.024
F)
PCx
CSNK2A1
p=0.861
G)
TCx
CSNK2A2
p=0.147
H)
HIP
CSNK2A2
p=0.365
Log2 intensity
NCI
Dementia
I)
#2♀
#3♀
#7♂
#5♂
C FTD C FTD C FTD C FTD
CK2α'
GAPDH
Age: 60 60 68 68 71 71 70 70
Tau pathology: - + - + - + n/a -
J)
CK2α' protein levels relative to matched control
Control
FTD
K)
CK2α' intensity (normalized to GAPDH)
FTD 1
FTD 7
Control 1
FTD 2
FTD 6
FTD 3
FTD 5
Control 6
FTD 4
Control 2
Control 3
Control 7
Control 4
Yes
No
Tau Pathology (NBB)

Figure 1

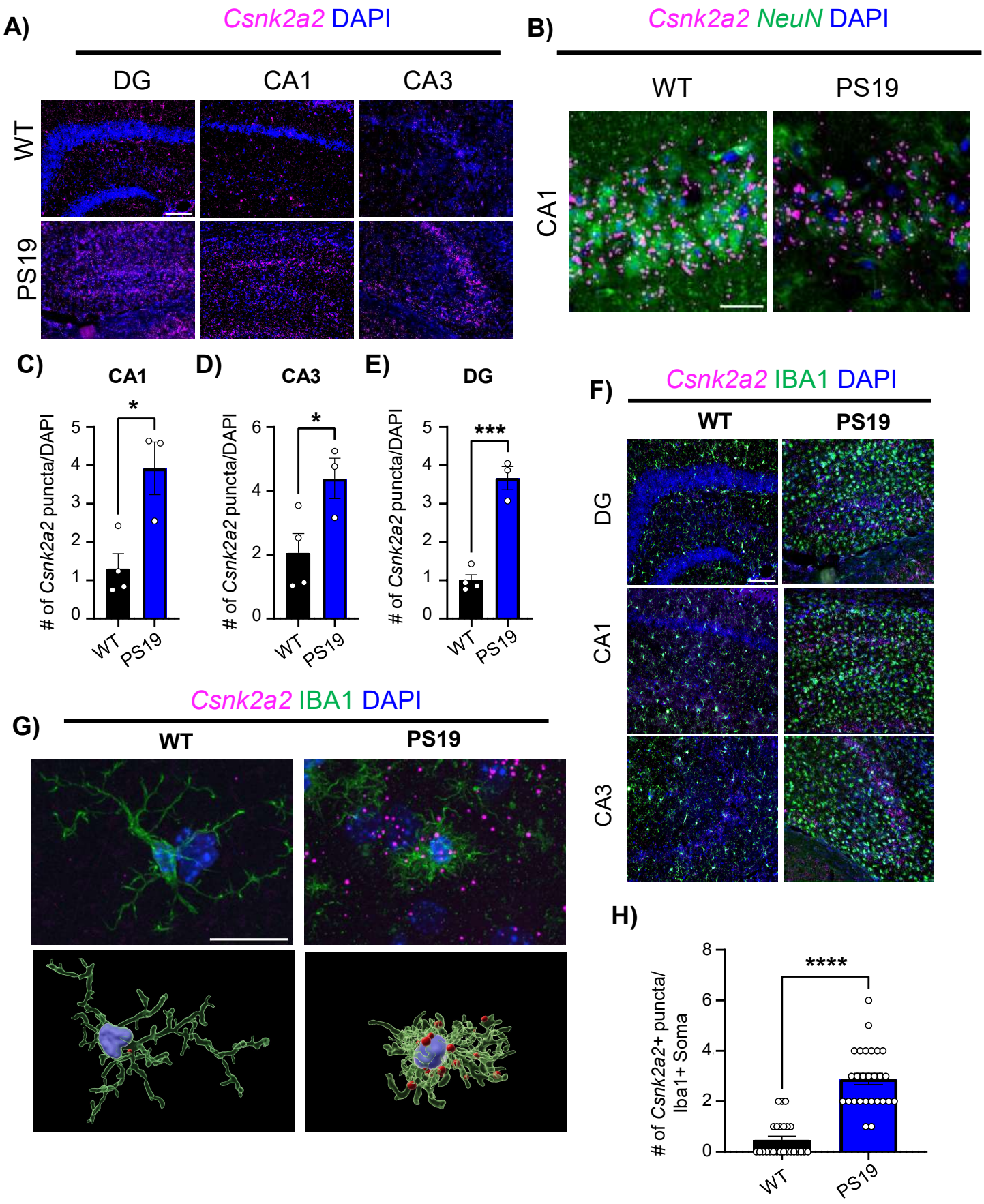
A)
Csnk2a2 DAPI
DG
CA1
CA3
WT
PS19
B)
Csnk2a2 NeuN DAPI
WT
PS19
CA1
C)
CA1
D)
CA3
E)
DG
# of Csnk2a2 puncta/DAPI
WT
PS19
F)
Csnk2a2 IBA1 DAPI
WT
PS19
DG
CA1
CA3
G)
Csnk2a2 IBA1 DAPI
WT
PS19
H)
# of Csnk2a2+ puncta/ Iba1+ Soma
WT
PS19

Figure 2

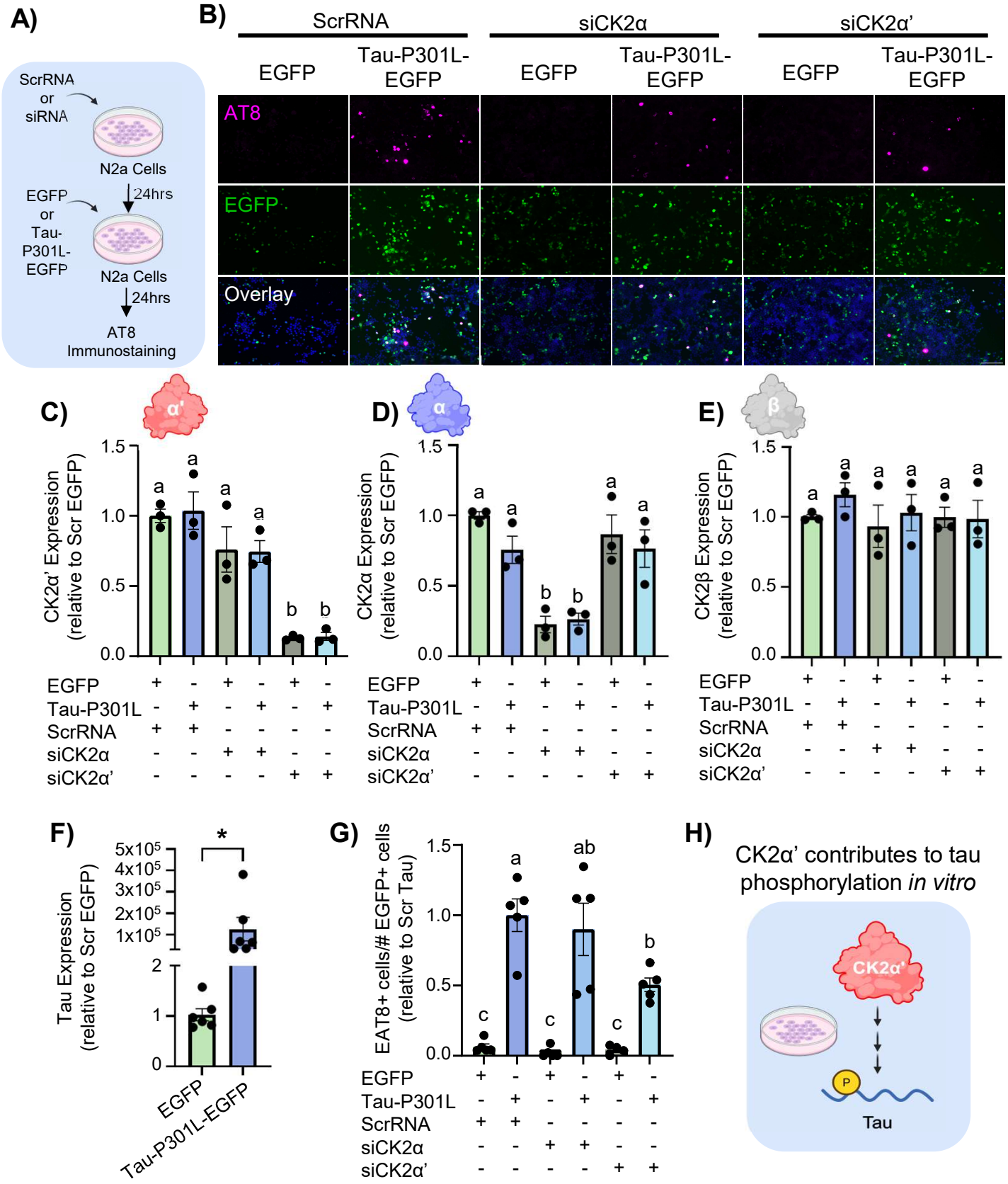
A)
ScrRNA or siRNA
N2a Cells
24hrs
EGFP or Tau-P301L-EGFP
N2a Cells
24hrs
AT8 Immunostaining
B)
ScrRNA
siCK2α
siCK2α'
EGFP
Tau-P301L-EGFP
AT8
EGFP
Overlay
C)
α'
CK2α' Expression (relative to Scr EGFP)
D)
α
CK2α Expression (relative to Scr EGFP)
E)
β
CK2β Expression (relative to Scr EGFP)
EGFP
Tau-P301L
ScrRNA
siCK2α
siCK2α'
F)
Tau Expression (relative to Scr EGFP)
EGFP
Tau-P301L-EGFP
G)
EAT8+ cells/# EGFP+ cells (relative to Scr Tau)
H)
CK2α' contributes to tau phosphorylation in vitro
CK2α'
P
Tau

Figure 3

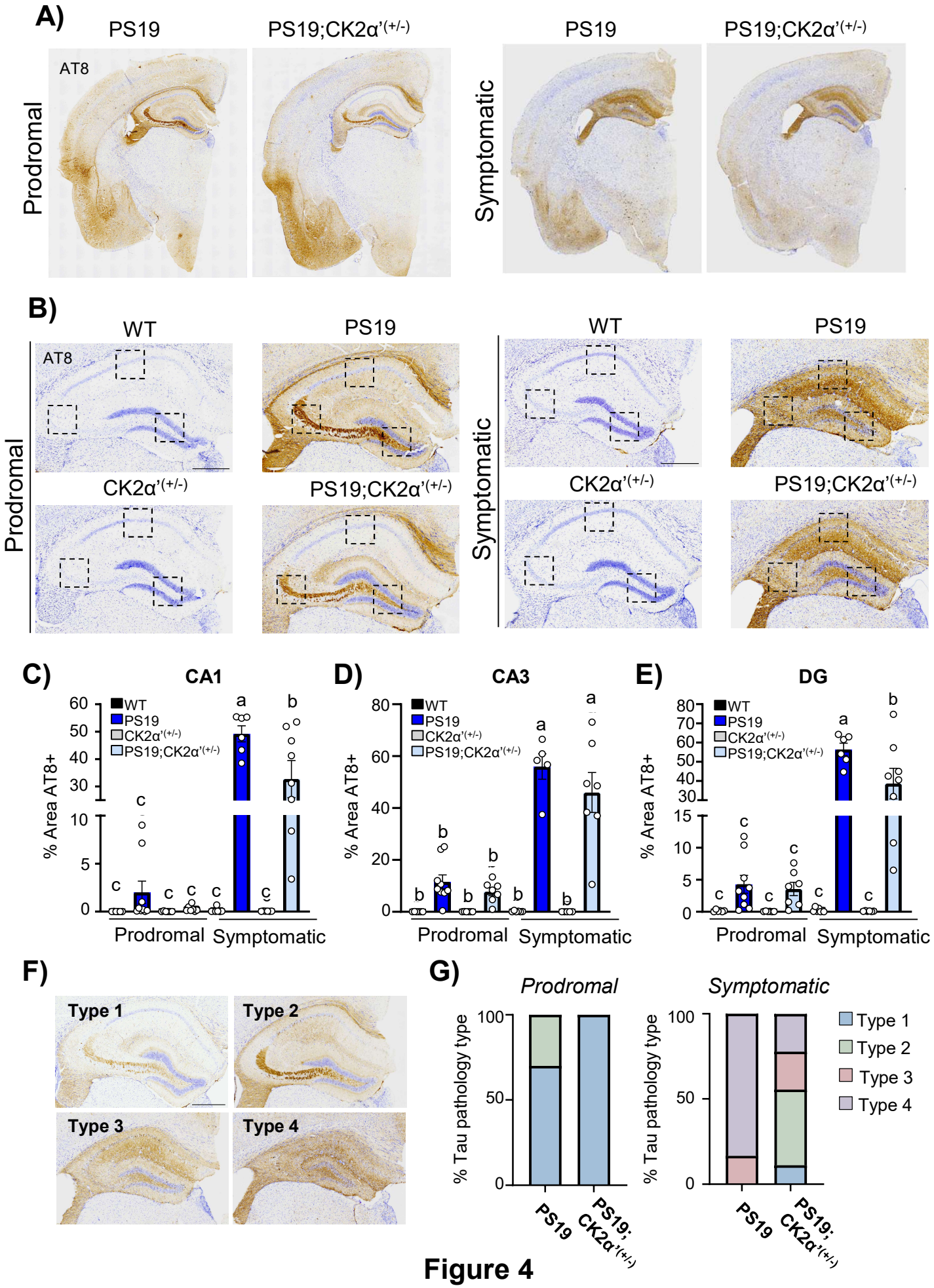
A)
PS19
PS19;CK2α'(+/-)
PS19
PS19;CK2α'(+/-)
AT8
Prodromal
Symptomatic
B)
WT
PS19
WT
PS19
AT8
CK2α'(+/-)
PS19;CK2α'(+/-)
CK2α'(+/-)
PS19;CK2α'(+/-)
Prodromal
Symptomatic
C)
CA1
D)
CA3
E)
DG
WT
PS19
CK2α'(+/-)
PS19;CK2α'(+/-)
% Area AT8+
Prodromal
Symptomatic
F)
Type 1
Type 2
Type 3
Type 4
G)
Prodromal
Symptomatic
% Tau pathology type
PS19
PS19; CK2α'(+/-)
Type 1
Type 2
Type 3
Type 4

Figure 4

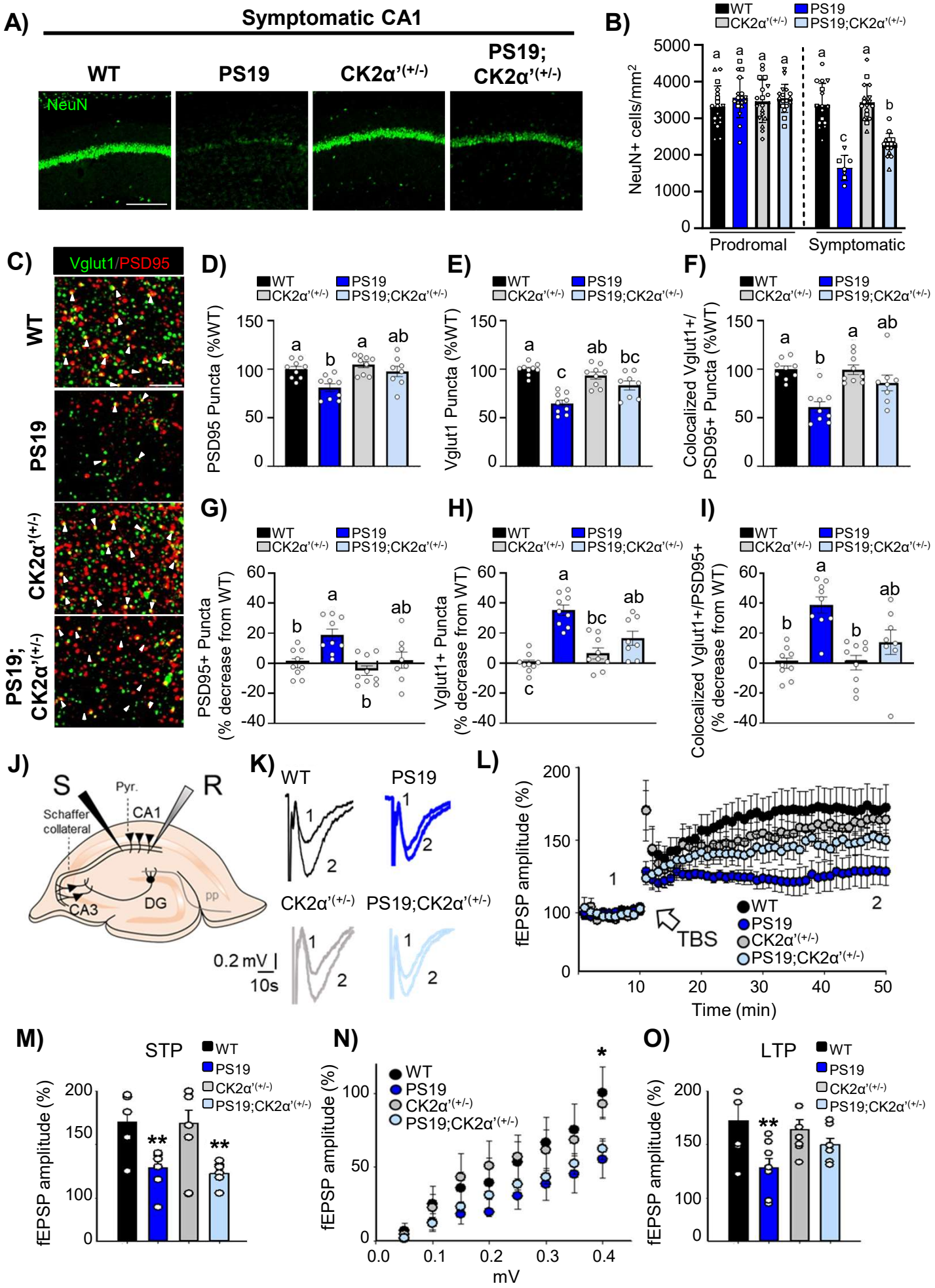
A)
Symptomatic CA1
WT
PS19
CK2α'(+/-)
PS19; CK2α'(+/-)
NeuN
B)
WT
PS19
CK2α'(+/-)
PS19;CK2α'(+/-)
NeuN+ cells/mm2
Prodromal
Symptomatic
C)
Vglut1/PSD95
WT
PS19
CK2α'(+/-)
PS19; CK2α'(+/-)
D)
PSD95 Puncta (%WT)
E)
Vglut1 Puncta (%WT)
F)
Colocalized Vglut1+/ PSD95+ Puncta (%WT)
G)
PSD95+ Puncta (% decrease from WT)
H)
Vglut1+ Puncta (% decrease from WT)
I)
Colocalized Vglut1+/PSD95+ (% decrease from WT)
J)
S
R
Pyr.
CA1
Schaffer collateral
CA3
DG
pp
K)
WT
PS19
CK2α'(+/-)
PS19;CK2α'(+/-)
0.2 mV
10s
L)
fEPSP amplitude (%)
TBS
Time (min)
M)
STP
fEPSP amplitude (%)
N)
fEPSP amplitude (%)
mV
O)
LTP
fEPSP amplitude (%)

Figure 5

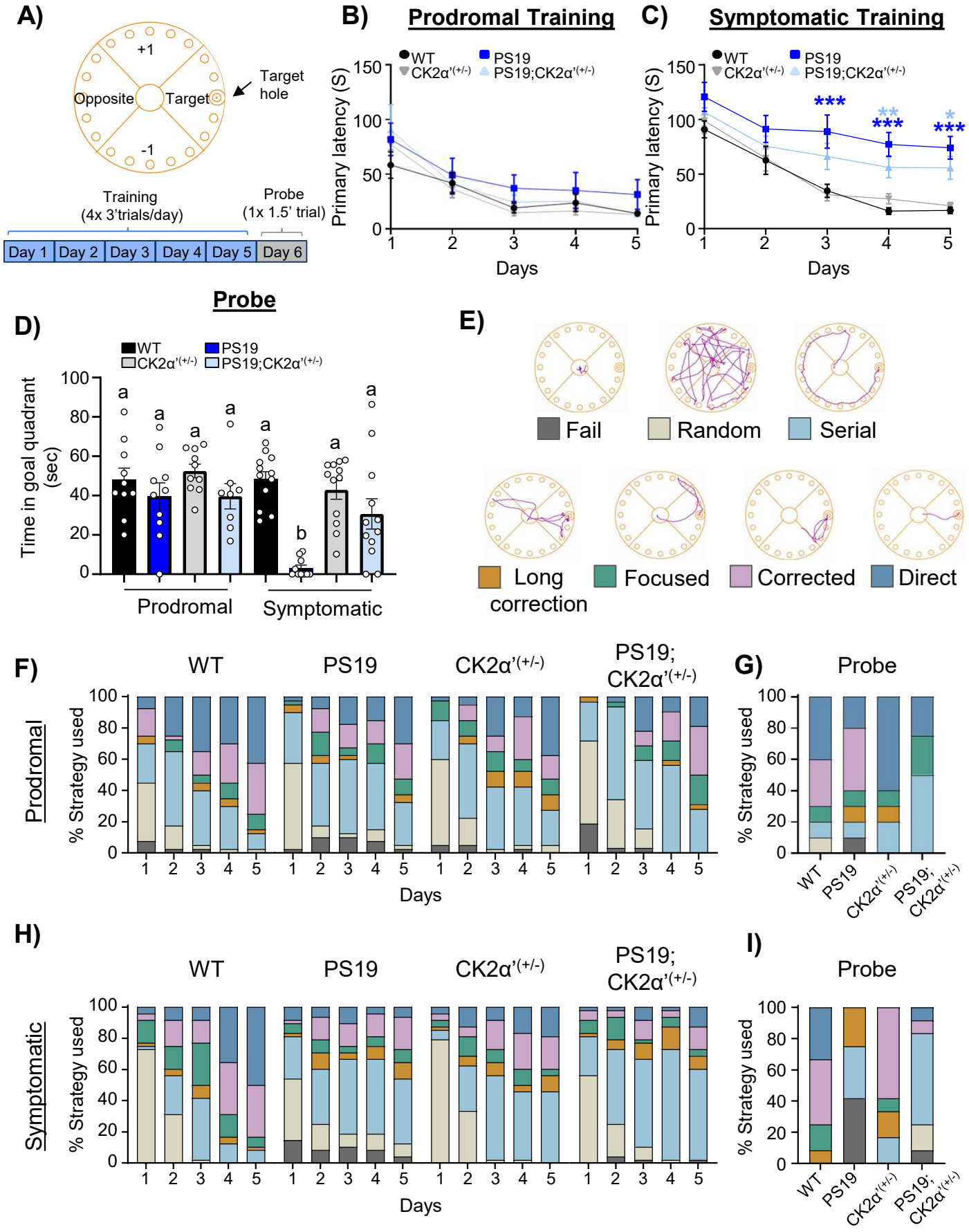
A)
+1
Opposite
Target
-1
Target hole
Training (4x 3'trials/day)
Probe (1x 1.5' trial)
Day 1
Day 2
Day 3
Day 4
Day 5
Day 6
B) Prodromal Training
C) Symptomatic Training
WT
PS19
CK2α'(+/-)
PS19;CK2α'(+/-)
Primary latency (S)
Days
D) Probe
Time in goal quadrant (sec)
Prodromal
Symptomatic
E)
Fail
Random
Serial
Long correction
Focused
Corrected
Direct
F)
G)
H)
I)
% Strategy used
Probe

Figure 6

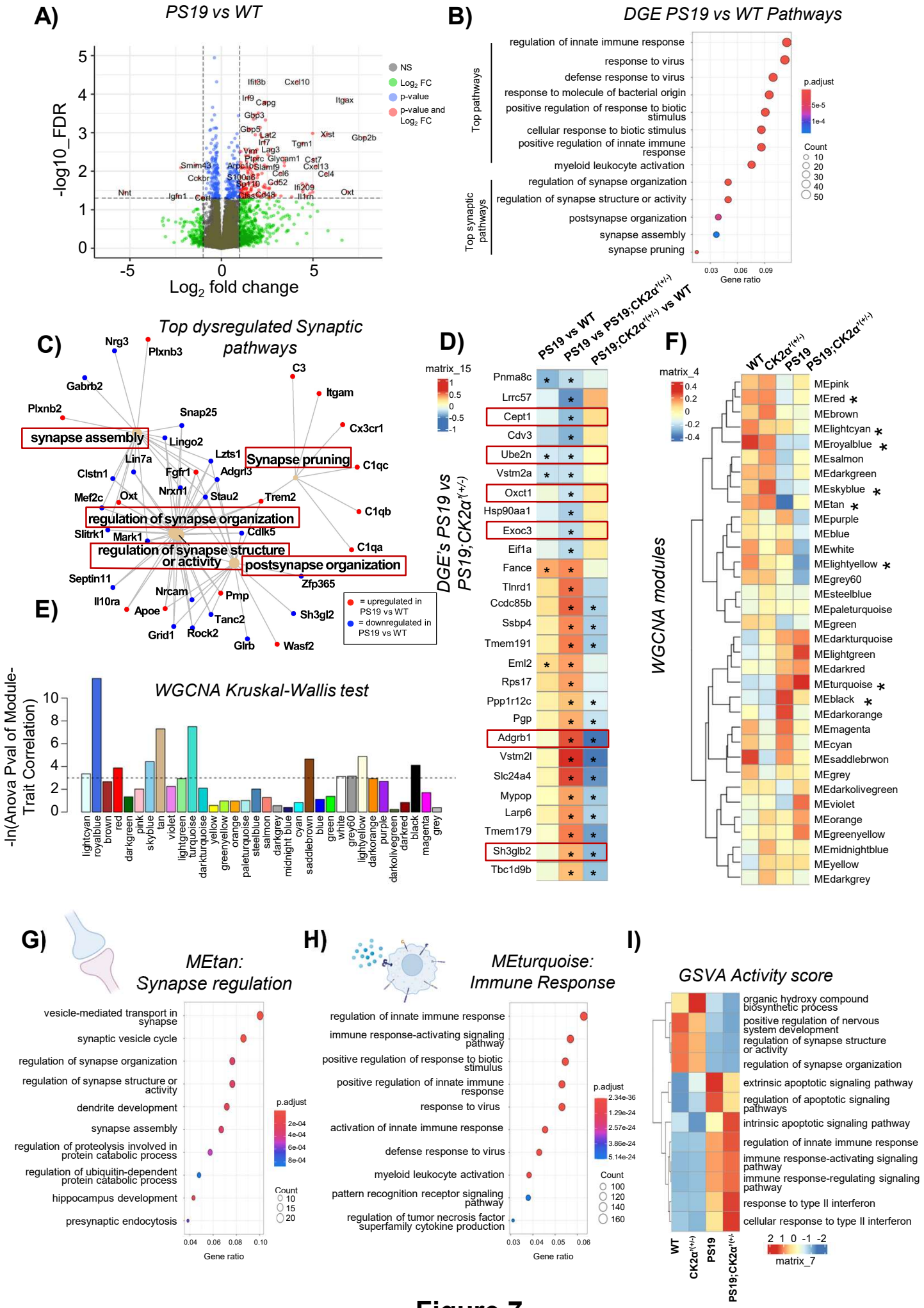
A)
PS19 vs WT
-log10_FDR
Log2 fold change
NS
Log2 FC
p-value
p-value and Log2 FC
B)
DGE PS19 vs WT Pathways
Top pathways
Top synaptic pathways
regulation of innate immune response
response to virus
defense response to virus
response to molecule of bacterial origin
positive regulation of response to biotic stimulus
cellular response to biotic stimulus
positive regulation of innate immune response
myeloid leukocyte activation
regulation of synapse organization
regulation of synapse structure or activity
postsynapse organization
synapse assembly
synapse pruning
Gene ratio
p.adjust
Count
C)
Top dysregulated Synaptic pathways
synapse assembly
Synapse pruning
regulation of synapse organization
regulation of synapse structure or activity
postsynapse organization
= upregulated in PS19 vs WT
= downregulated in PS19 vs WT
D)
DGE's PS19 vs PS19;CK2α(+/-)
PS19 vs WT
PS19 vs PS19;CK2α(+/-)
PS19;CK2α(+/-) vs WT
matrix_15
E)
WGCNA Kruskal-Wallis test
-ln(Anova Pval of Module-Trait Correlation)
F)
WGCNA modules
WT
CK2α(+/-)
PS19
PS19;CK2α(+/-)
matrix_4
G)
MEtan: Synapse regulation
vesicle-mediated transport in synapse
synaptic vesicle cycle
regulation of synapse organization
regulation of synapse structure or activity
dendrite development
synapse assembly
regulation of proteolysis involved in protein catabolic process
regulation of ubiquitin-dependent protein catabolic process
hippocampus development
presynaptic endocytosis
H)
MEturquoise: Immune Response
regulation of innate immune response
immune response-activating signaling pathway
positive regulation of response to biotic stimulus
positive regulation of innate immune response
response to virus
activation of innate immune response
defense response to virus
myeloid leukocyte activation
pattern recognition receptor signaling pathway
regulation of tumor necrosis factor superfamily cytokine production
I)
GSVA Activity score
organic hydroxy compound biosynthetic process
positive regulation of nervous system development
regulation of synapse structure or activity
regulation of synapse organization
extrinsic apoptotic signaling pathway
regulation of apoptotic signaling pathways
intrinsic apoptotic signaling pathway
regulation of innate immune response
immune response-activating signaling pathway
immune response-regulating signaling pathway
response to type II interferon
cellular response to type II interferon
matrix_7

Figure 7

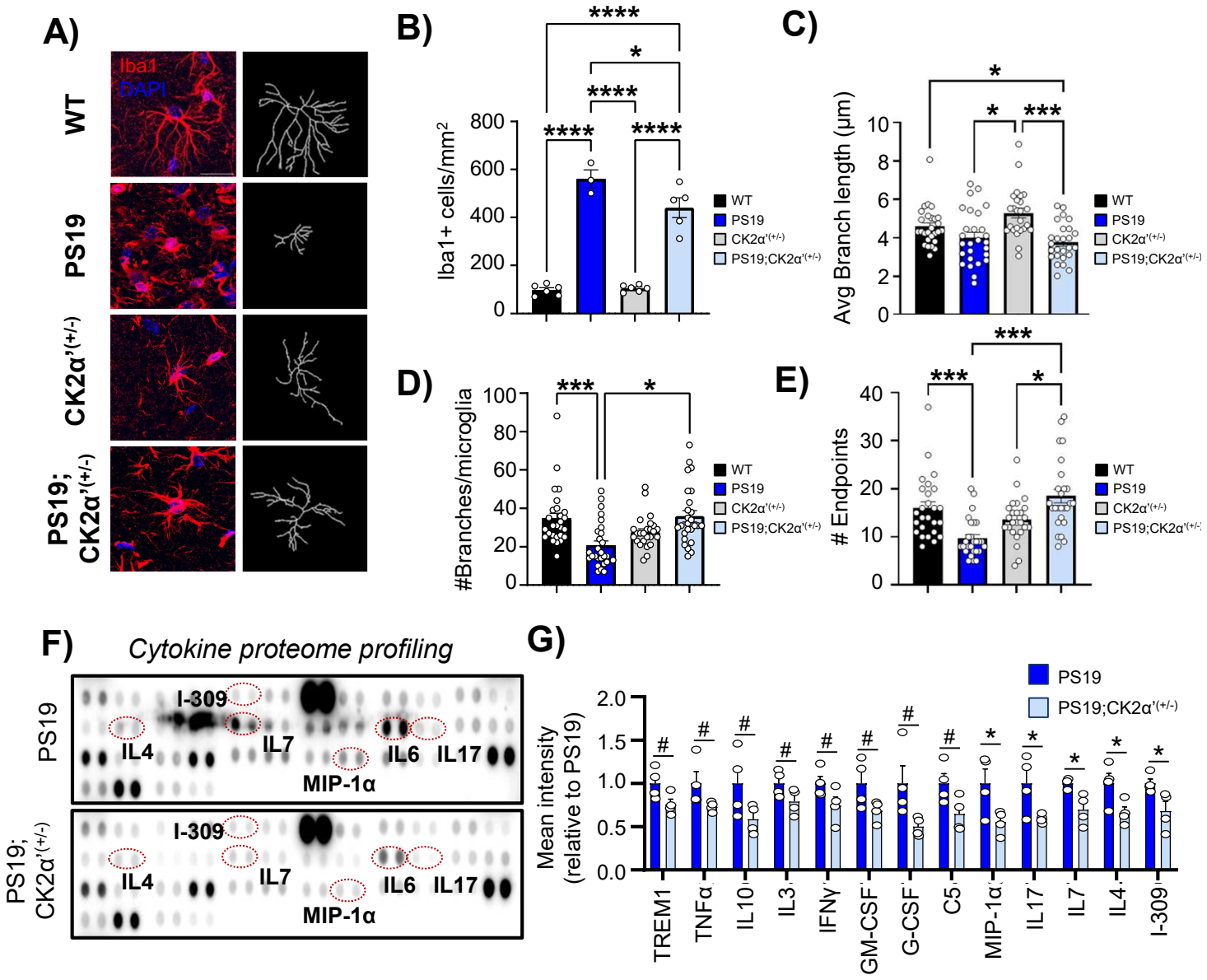
A)
Iba1
DAPI
WT
PS19
CK2α'(+/-)
PS19; CK2α'(+/-)
B)
Iba1+ cells/mm²
800
600
400
200
0
****
*
****
****
****
WT
PS19
CK2α'(+/-)
PS19;CK2α'(+/-)
C)
Avg Branch length (μm)
10
8
6
4
2
0
*
*
***
WT
PS19
CK2α'(+/-)
PS19;CK2α'(+/-)
D)
#Branches/microglia
100
80
60
40
20
0
***
*
WT
PS19
CK2α'(+/-)
PS19;CK2α'(+/-)
E)
Endpoints
40
30
20
10
0
***
***
*
WT
PS19
CK2α'(+/-)
PS19;CK2α'(+/-)
F)
Cytokine proteome profiling
PS19
PS19; CK2α'(+/-)
I-309
IL4
IL7
IL6
IL17
MIP-1α
G)
PS19
PS19;CK2α'(+/-)
Mean intensity (relative to PS19)
2.0
1.5
1.0
0.5
0.0
TREM1
TNFα
IL10
IL3
IFNγ
GM-CSF
G-CSF
C5
MIP-1α
IL17
IL7
IL4
I-309

Figure 8

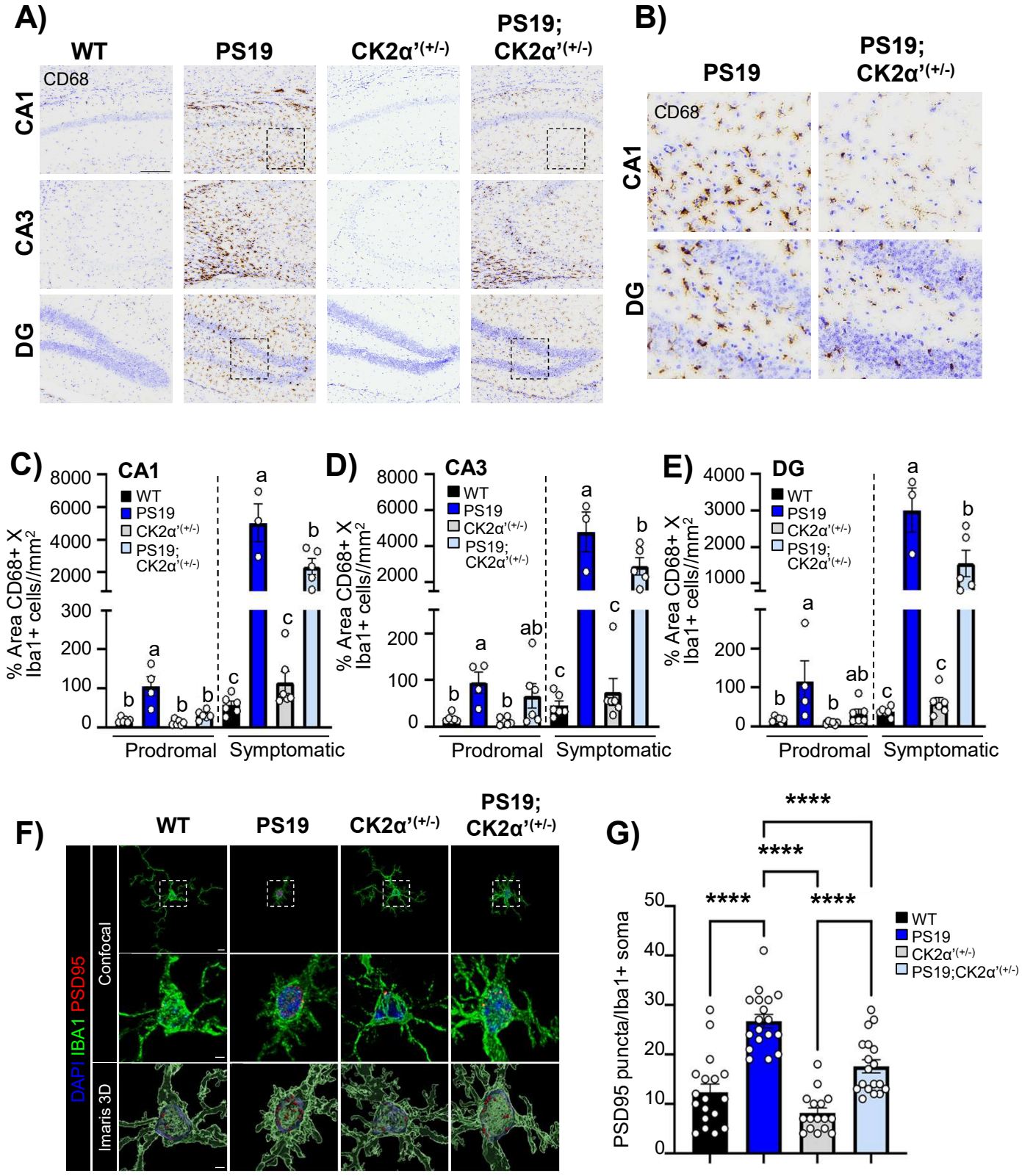
A)
WT
PS19
CK2α'(+/-)
PS19; CK2α'(+/-)
CD68
CA1
CA3
DG
B)
PS19
PS19; CK2α'(+/-)
CD68
CA1
DG
C)
CA1
D)
CA3
E)
DG
WT
PS19
CK2α'(+/-)
PS19; CK2α'(+/-)
% Area CD68+ X Iba1+ cells//mm²
Prodromal
Symptomatic
F)
WT
PS19
CK2α'(+/-)
PS19; CK2α'(+/-)
DAPI IBA1 PSD95
Confocal
Imaris 3D
G)
PSD95 puncta/Iba1+ soma
WT
PS19
CK2α'(+/-)
PS19;CK2α'(+/-)
****

Figure 9